

# AMICO galaxy clusters in KiDS-DR3: the impact of estimator statistics on the luminosity-mass scaling relation

Merijn Smit<sup>1\*</sup>, Andrej Dvornik<sup>2,1</sup>, Mario Radovich<sup>3</sup>, Konrad Kuijken<sup>1</sup>, Matteo Maturi<sup>4</sup>, Lauro Moscardini<sup>5,6,7</sup>, and Mauro Sereno<sup>6,7</sup>

<sup>1</sup> Leiden Observatory, Leiden University, PO Box 9513, 2300RA Leiden, The Netherlands

<sup>2</sup> Ruhr University Bochum, Faculty of Physics and Astronomy, Astronomical Institute (AIRUB), German Centre for Cosmological Lensing, 44780 Bochum, Germany

<sup>3</sup> INAF - Osservatorio Astronomico di Padova, vicolo dell'Osservatorio 5, Padova 35122, Italy

<sup>4</sup> Zentrum für Astronomie, Universität Heidelberg, Philosophenweg 12, D-69120 Heidelberg, Germany

<sup>5</sup> Dipartimento di Fisica e Astronomia "Augusto Righi" - Alma Mater Studiorum Università di Bologna, via Piero Gobetti 93/2, I-40129 Bologna, Italy

<sup>6</sup> INAF - Osservatorio di Astrofisica e Scienza dello Spazio di Bologna, via Gobetti Piero 93/3, I-40129 Bologna, Italy

<sup>7</sup> INFN - Sezione di Bologna, viale Berti Pichat 6/2, I-40127 Bologna, Italy

Received <date> / Accepted <date>

## ABSTRACT

**Context.** As modern-day precision cosmology aims for statistical uncertainties of the percent level or lower, it becomes increasingly important to reconsider estimator assumptions at each step of the process, and their consequences on the statistical variability of the scientific results.

**Aims.** We compare  $L^1$  regression statistics to the weighted mean, the canonical  $L^2$  method based on Gaussian assumptions, for inference of the weak gravitational shear signal from a catalog of background ellipticity measurements around a sample of clusters, in many recent analyses a standard step in the process.

**Methods.** We use the shape measurements of background sources around 6925 AMICO clusters detected in the KiDS 3rd data release. We investigate the robustness of our results and the dependence of uncertainties on the signal-to-noise ratios of the background source detections. Using a halo model approach, we derive lensing masses from the estimated excess surface density profiles.

**Results.** The highly significant shear signal allows us to study the scaling relation between the  $r$ -band cluster luminosity  $L_{200}$ , and the derived lensing mass  $M_{200}$ . We show the results of the scaling relations derived in 13 bins in  $L_{200}$ , with a tightly constrained power law slope of  $\sim 1.24 \pm 0.08$ . We observe a small, but significant relative bias of a few percent in the recovered excess surface density profiles between the two regression methods, which translates to a  $1\sigma$  difference in  $M_{200}$ . The efficiency of  $L^1$  is at least that of the weighted mean, relatively increasing with higher signal-to-noise shape measurements.

**Conclusions.** Our results indicate the relevance of optimizing the estimator for inferring the gravitational shear from a distribution of background ellipticities. The interpretation of measured relative biases can be gauged by deeper observations, while increased computation times remain feasible.

**Key words.** gravitational lensing: weak – galaxies: clusters: general – galaxies: groups: general – methods: statistical – cosmology: large scale structure – methods: data analysis

## 1. Introduction

Statistics is an essential part of astronomy (Heck et al. 1985; Feigelson 1988, 2009; Feigelson & Babu 2013). The field relies on inferring physical properties, that cannot be determined directly, from observable quantities, which in turn need to be corrected for systematic effects, and instrumental and observational biases.

The key question remains always, when interpreting observations and results, what one is actually seeing, before discussing how accurately these results can be constrained.

Weak gravitational lensing, caused by the deflection of light rays by density variations along the traveled path, has been a case in point for the last three decades. Gravitational lensing is a convex focusing effect, that can magnify and shear affected background sources. The *observed* shapes and number counts

can conversely yield information about these density variations, but need to be disentangled statistically from the unknown *intrinsic* properties of background sources, such as distance, size (and luminosity), and shape.

Since the first detections of coherent alignments of galaxy shapes in the background of clusters (Tyson et al. 1990), the emerging fields of galaxy-galaxy lensing, where the lensing ‘structure’ is itself an ensemble of lenses (Brainerd et al. 1996), and cosmic shear, the weak lensing induced by large-scale structure (Wittman et al. 2000; Bacon et al. 2000; Kaiser et al. 2000; Van Waerbeke et al. 2000), techniques have progressed rapidly and demands on accuracy have become increasingly stringent.

This is the second of a set of papers, wherein we focus on the statistical aspects of inferring the lensing signal from the intrinsic shapes and the estimated lensing geometry, which depends on the distances between the observer, the moment of deflection and the background sources. Assuming the cosmological prin-

\* e-mail: msmit@strw.leidenuniv.nl

ple, the intrinsic shapes of a sample<sup>1</sup> of background galaxies, including their orientation, are random, and the intrinsic galaxy shapes should average out from a sufficiently large sample, leaving the weak lensing signal as a net ellipticity. The common approach has been to take a weighted mean of galaxy ellipticities, which has computational and analytical advantages and, most importantly, is an unbiased estimator of the shear in the absence of pixel noise in the galaxy images (Seitz & Schneider 1997).

However, in practice there are many sources of noise and the mean is known to be biased, underestimating the underlying shear signal (Melchior & Viola 2012; Viola et al. 2014; Sellentin et al. 2018; Mandelbaum 2018).

The distribution of intrinsic galaxy shapes is well known to be non-Gaussian (Lambas et al. 1992; Rodríguez & Padilla 2013), and in fact centrally peaked. In Smit & Kuijken (2018, hereafter Paper I), we explored alternative estimators besides the mean, that could potentially be better suited for such a cuspy distribution. It was found, using realistic simulated distributions and resampling of CFHTLenS shape measurements (Heymans et al. 2012), that  $L^1$ -norm regression, also known as least absolute deviations (LAD), reduces bias from between  $\sim -4\%$  and  $\sim -4.5\%$  to between  $\sim +1\%$  and  $\sim -3\%$ , while at the same time reducing uncertainty by  $\sim 9\%$  to  $\sim 23\%$ .

In this paper, we extend this study by applying these statistics to a weak lensing analysis of 6925 galaxy clusters in the AMICO cluster catalog (Bellagamba et al. 2011; Radovich et al. 2017; Bellagamba et al. 2018; Maturi et al. 2019; Bellagamba et al. 2019) of the 3rd KiDS data release (de Jong et al. 2017). As opposed to Paper I, in this case the true lensing signal (here in the form of the excess surface density of the clusters) is unknown. We therefore study the relative biases and uncertainties between LAD and the mean, and compare results to our findings in Paper I.

An important application is then to study the relation between observable properties of clusters and groups and physical quantities derived from the lensing signal, i.e. the matter distribution, to better our understanding of galaxy and cluster formation and cosmological models (e.g. Kautsch et al. 2008; Leauthaud et al. 2010; Lesci et al. in prep.). We calculate halo masses from the obtained lensing signals and derive a scaling relation between the observed  $r$ -band luminosity and the lensing mass, investigating the impact of estimator choice on the resulting constraints.

The order of magnitude of this estimated bias in the weak lensing results can be dominant, compared to other sources of uncertainty in the process. Developments in the field have led to current constraints of the multiplicative bias in shape measurements of the order of  $\sim 1\%$  (Bernstein & Jarvis 2002; Hirata & Seljak 2003; Heymans et al. 2006; Massey et al. 2007; Miller et al. 2007; Kitching et al. 2008; Bridle et al. 2010; Voigt & Bridle 2010; Bernstein 2010; Kitching et al. 2012; Kacprzak et al. 2012; Melchior & Viola 2012; Refregier et al. 2012; Heymans et al. 2012; Mandelbaum et al. 2015; Viola et al. 2015; Fenech Conti et al. 2017). The uncertainty in the lensing geometry between observer, lens and background sources, introduced by the estimation of the photometric redshift probability distributions, can be a few percent (Hildebrandt et al. 2017; Bellagamba et al. 2019, and Appendix A.1). The broad category of selection biases, e.g. introduced by intrinsic alignments, contamination of the background sample by cluster member galaxies, blending, detection and subsequent selection effects, typically accumulate

up to a few percent (Miyatake et al. 2015; van Uitert et al. 2017; Bellagamba et al. 2019) for cluster weak lensing. For instance, estimations on background selection yield a foreground contamination of the order of 2%, which can be partly corrected for, but does increase the uncertainty (Dvornik et al. 2017; Bellagamba et al. 2019, and Appendix A.2). In this study, we investigate the usability of background sources to smaller radii than in Bellagamba et al. (2019).

These demands on accuracy and precision become higher as the data yield and therefore the statistical power of surveys increase dramatically (Mandelbaum 2018), as achieved by COSMOS<sup>2</sup> (Leauthaud et al. 2007), CFHTLenS<sup>3</sup> (Heymans et al. 2012), RCSLenS<sup>4</sup> (Hildebrandt et al. 2016), KiDS<sup>5</sup> (de Jong et al. 2013), DES<sup>6</sup> (Dark Energy Survey Collaboration et al. 2016), and foreseen for future surveys like LSST<sup>7</sup> (Ivezić et al. 2019), Euclid<sup>8</sup> (Laureijs et al. 2011). While these future surveys will require constraints on systematic uncertainty of order  $\leq 2 \times 10^{-3}$  (Mandelbaum 2018), we show that even for weak lensing analyses in the last decade, the bias in shear inference can dominate other sources, such as the aforementioned multiplicative shape measurement bias, that is commonly corrected for as in Viola et al. (2015); Dvornik et al. (2017); Bellagamba et al. (2019).

Several other approaches have been made to address this, including analytic modeling of the bias (e.g. Viola et al. 2014), weight corrections and priors (Bonnet & Mellier 1995; Van Waerbeke et al. 2000; Bernstein & Jarvis 2002) or nulling techniques (Herbonnet et al. 2017). Calculating the main observable, the shapes of lensed background sources, relies itself on statistical methods. These are based mainly on surface brightness moments (Kaiser et al. 1995; Rhodes et al. 2000) or model fitting (Kuijken 1999; Bernstein & Jarvis 2002; Hirata & Seljak 2003; Refregier & Bacon 2003; Kuijken 2006; Miller et al. 2007; Kitching et al. 2008). This means the most common approaches are corrections on a statistic that remains fundamentally skewed (Sellentin et al. 2018; Mandelbaum 2018).

Promising alternative approaches by Bernstein & Armstrong (2014); Schneider et al. (2015) do not reproduce individual background shapes, but directly determine the underlying shear field from ensembles of background sources, reconsidering these steps in the chain of statistical inference. While future lensing surveys will require innovative improvements, these methods and their priors need to be gauged by deep observations of high signal-to-noise, and it is of fundamental importance that these calibrations are well constrained and do not suffer from even subtle systematic biases. In other words, the comparison of several perspectives is paramount in determining what we actually see.

The remainder of this paper is organized as follows. We will introduce the definitions of galaxy shapes and the weak lensing formalism in Section 2, and relate these to our statistical approach. Data, analysis methods and selection criteria are described in Section 3, while Section 4 states our results and analysis. Section 5 gives a summary of our conclusions.

Throughout this paper we assume a Planck (Planck Collaboration et al. 2014) cosmology with  $\Omega_M = 0.315$ ,  $\Omega_\Lambda = 0.685$  and

<sup>2</sup> <http://cosmos.astro.caltech.edu/>

<sup>3</sup> <http://www.cfhtlens.org>

<sup>4</sup> <http://www.rcslens.org/>

<sup>5</sup> <http://kids.strw.leidenuniv.nl/>

<sup>6</sup> <http://www.darkenergysurvey.org/>

<sup>7</sup> <https://www.lsst.org/>

<sup>8</sup> <http://www.euclid-ec.org/>

<sup>1</sup> There are several considerations involved in the proper selection of such a sample, explained in Sections 2 and 3.

$H_0 = 100.0 h \text{ km s}^{-1} \text{ Mpc}^{-1}$ . All measurements are in comoving units, unless specifically noted otherwise, such as in Section 2.

## 2. Weak gravitational lensing statistics

We briefly review the principles of weak gravitational lensing and relate the central concepts to our statistical approach, introducing terminology and notation conventions used in this paper, while referring the reader to excellent reviews such as Bartelmann & Schneider (2001); Schneider (2006); Hoekstra & Jain (2008); Bartelmann & Maturi (2017), for more in-depth approaches.

### 2.1. Principles of weak lensing

Rays of light are deflected by the curvature or space-time due to mass inhomogeneities along their path. A mass overdensity acts as a convex lens on the light rays from distant sources behind that lens to an observer. In this paragraph, we use angular-diameter distances  $D_l$  from observer to lens,  $D_{ls}$  from lens to background source, and  $D_s$  from observer to background source (see Fig 1), and translate quantities to comoving units where necessary for the remainder of this paper.

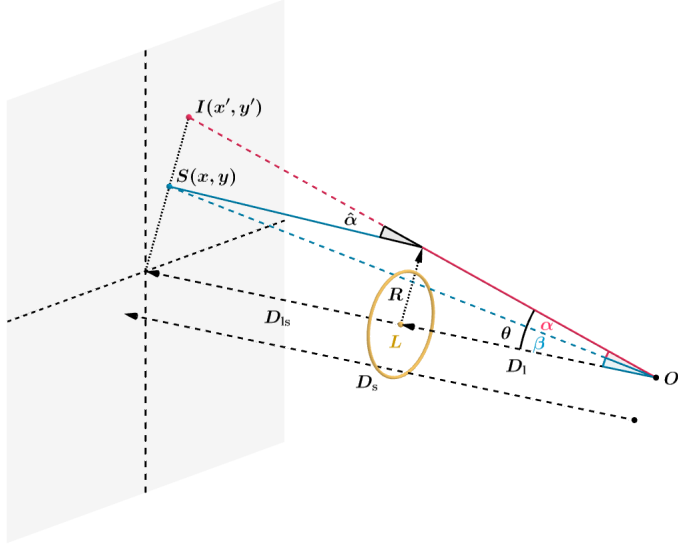


**Fig. 1.** Representation of a gravitational lens system, showing the displacement of a source at position  $S(x, y)$  to an image at position  $I(x', y')$ , where we take the origin of the source plane collinear with the position of the lens  $L$  and the observer  $O$ .

For the purposes of this work, the extent of the lensing mass along the line of sight, compared to the distances from observer to lens and from lens to background source, can be considered negligible. In this so-called thin-lens approximation, the deflection of light rays by a deflection angle  $\hat{\alpha}$  leads to an effective angular displacement (again see Fig. 1)

$$\alpha = -\frac{D_{ls}}{D_s} \hat{\alpha}, \quad (1)$$

also called the reduced deflection angle, relating the observed position  $\theta$  of a distant point source to its unlensed position  $\beta$  by the lens equation

$$\beta = \theta - \alpha. \quad (2)$$

It can be shown through the relation between  $\hat{\alpha}$  and the three-dimensional gravitational potential  $\Phi$ , that this displacement is then described by  $\alpha = \nabla_\theta \psi$ , where

$$\psi = \frac{2}{c^2} \frac{D_{ls}}{D_l D_s} \int \Phi dz \quad (3)$$

is called the (two-dimensional) lensing potential.

The differential effect of the deflection of light on the images  $I(x, y)$  of extended background sources can to first order be described as a coordinate transformation, by taking the derivatives in the lens equation (2) of the original angular position  $\beta$  with respect to the observed position  $\theta$ . Substituting  $\nabla_\theta \psi$  for  $\alpha$ , we obtain the Jacobian matrix:

$$\begin{pmatrix} x' \\ y' \end{pmatrix} = \begin{pmatrix} 1 - \psi_{11} & -\psi_{12} \\ -\psi_{21} & 1 - \psi_{22} \end{pmatrix} \begin{pmatrix} x \\ y \end{pmatrix}, \quad (4)$$

with

$$\psi_{ij} = \frac{\partial^2 \psi}{\partial \theta_i \partial \theta_j}, \quad (5)$$

resulting in the lensed image  $I(x', y')$ , which is the key observable in our weak lensing study.

#### 2.1.1. Critical surface mass density

To interpret the effect on the source image, we note that such a transformation can be decomposed in three parts, namely the identity  $I$ , an isotropic part describing a multiplication, and an anisotropic, traceless part, describing a shearing of the image:

$$I - \frac{1}{2}(\psi_{11} + \psi_{22})I + \begin{pmatrix} -\frac{1}{2}(\psi_{11} - \psi_{22}) & -\psi_{12} \\ -\psi_{21} & \frac{1}{2}(\psi_{11} - \psi_{22}) \end{pmatrix} \quad (6)$$

To relate  $\psi_{ij}$  with the density of the lensing mass, we start with the isotropic term, which is half the Laplacian of the lensing potential:  $\frac{1}{2}(\psi_{11} + \psi_{22}) = \frac{1}{2} \nabla_\theta^2 \psi$ . From equation 3, we obtain

$$\frac{1}{2} \nabla_\theta^2 \psi = \frac{1}{c^2} \frac{D_l D_{ls}}{D_s} \int 4\pi G \rho dz, \quad (7)$$

which is a dimensionless quantity. Defining the surface mass density as

$$\Sigma \equiv \int \rho dz \quad (8)$$

and gathering the rest of the right-hand side into

$$\frac{4\pi G}{c^2} \frac{D_l D_{ls}}{D_s} \equiv \Sigma_{cr}^{-1}, \quad (9)$$

with  $\Sigma_{cr}$  called the critical surface mass density, we find that the isotropic term can be written as

$$\kappa \equiv \frac{1}{2} \nabla_\theta^2 \psi = \frac{\Sigma}{\Sigma_{cr}}, \quad (10)$$

with  $\kappa$  a normalized dimensionless surface mass density. Recognizing that  $\nabla_\theta^2 \psi = \nabla \cdot \alpha$  is the divergence of the deflection of the light rays, i.e. the manner in which those light rays converge due to the lensing effect,  $\kappa$  is simply called the convergence.

### 2.1.2. Shear and intrinsic ellipticity

The shear matrix in eq. 6 has two independent components, simply called the shear  $\gamma = \gamma_1 + i\gamma_2$ , with  $\gamma_1 = \frac{1}{2}(\psi_{11} - \psi_{22})$  and  $\gamma_2 = \psi_{12} = \psi_{21}$ . Eq. 4 then becomes

$$\begin{pmatrix} x' \\ y' \end{pmatrix} = \begin{pmatrix} 1 - \kappa - \gamma_1 & -\gamma_2 \\ -\gamma_2 & 1 - \kappa + \gamma_1 \end{pmatrix} \begin{pmatrix} x \\ y \end{pmatrix}. \quad (11)$$

This transformation leads to magnification and distortion of the light distribution of background sources. In this work, we focus on the most commonly used net distortion or reduced shear  $g = g_1 + ig_2 \equiv (\gamma_1 + i\gamma_2)/(1 - \kappa)$ :

$$\begin{pmatrix} x' \\ y' \end{pmatrix} = (1 - \kappa) \begin{pmatrix} 1 - g_1 & -g_2 \\ -g_2 & 1 + g_1 \end{pmatrix} \begin{pmatrix} x \\ y \end{pmatrix}, \quad (12)$$

where the transformation is written as a multiplication of  $(1 - \kappa)$  and a distortion matrix describing the alignment of lensed sources in the foreground potential.

The effect on a circular source is a shearing into an ellipse with axis ratio  $q = \frac{b}{a}$  as

$$q = \frac{1 - |g|}{1 + |g|} \Leftrightarrow |g| = \frac{1 - q}{1 + q} = \frac{a - b}{a + b}, \quad (13)$$

and position angle  $\varphi$  via

$$g = |g| (\cos 2\varphi + i \sin 2\varphi). \quad (14)$$

As mentioned before, we do not measure this gravitational distortion directly. Background sources have an intrinsic shape distribution and we effectively measure the combined effect of their intrinsic shape and a weak lensing distortion. It is adequate to describe images by their quadrupole brightness moments or their ellipticities, and the respective response to weak shear distortions. It is straightforward to use the common definition<sup>9</sup> of ellipticity, defined as the reduced shear needed to create the intrinsic shape  $\epsilon = \epsilon_1 + i\epsilon_2$  of a source from an image with circular isophotes (Bernstein & Jarvis 2002; Kuijken 2006). The resulting ellipticity  $\epsilon$ , after transforming an image with intrinsic<sup>10</sup> ellipticity  $\epsilon^I$  by a distortion  $g$ , is then given by (Seitz & Schneider 1997)

$$\epsilon = \frac{\epsilon^I + g}{1 + g^* \epsilon^I} \quad \text{for } |g| \leq 1, \quad (15)$$

with  $g^*$  the complex conjugate of  $g$ .

The intrinsic shape distribution is called shape noise and assuming no preferred direction on the sky, should average to zero:  $\langle \epsilon^I \rangle = 0$ . This way, each background shape measurement  $\epsilon$  is then an independent estimate of the underlying reduced shear  $g$ .

In this paper, we make use of the fact that the lensing signal is weak, i.e.  $\kappa \ll 1$ , and assume  $g \approx \gamma$ .

<sup>9</sup> An alternative definition of ellipticity is often denoted as  $|\chi| = \frac{1-q^2}{1+q^2}$ , related to the geometrical eccentricity, and called polarization (e.g. Seitz & Schneider 1995; Viola et al. 2014).

<sup>10</sup> We note that our notation differs from paper I. Here the measured ellipticity is denoted as  $\epsilon$ , instead of  $\bar{e}$  (paper I), and the intrinsic ellipticity is denoted  $\epsilon^I$ , instead of  $e$ .

### 2.2. Estimation of the surface density profile

The shear induced by gravitational lensing is sensitive to the density contrast. For an axisymmetric lens, we can write  $|\gamma|(R) = \bar{\kappa}(\leq R) - \kappa(R)$ , where  $\bar{\kappa}$  is the average convergence within radius  $R$ . In fact, this relation holds for other mass distributions if we average azimuthally around the lens. In this work, we study the stacked signal of many lenses and assume a net axisymmetry (see e.g. Evans & Bridle 2009; Oguri et al. 2010; Clampitt & Jain 2016; van Uitert et al. 2017, for weak lensing studies on elliptical lenses).

Since it can be seen from Fig. 1 that the gravitational shear acts in the radial direction, we define the tangential and cross components of the shear as

$$\begin{pmatrix} \gamma_+ \\ \gamma_\times \end{pmatrix} = \begin{pmatrix} -\cos(2\phi) & -\sin(2\phi) \\ \sin(2\phi) & -\cos(2\phi) \end{pmatrix} \begin{pmatrix} \gamma_1 \\ \gamma_2 \end{pmatrix}, \quad (16)$$

with  $\phi$  the counterclockwise angle between the positive  $x$ -axis<sup>11</sup> and the vector from lens to source. This gives

$$\bar{\Sigma}(\leq R) - \Sigma(R) \equiv \Delta\Sigma(R) = \gamma_+(R) \Sigma_{\text{cr}}, \quad (17)$$

with  $\Delta\Sigma(R)$  the excess surface density (ESD) at a radius  $R$  around the lensing mass. In axisymmetric lenses, the cross component of the shear cannot arise from gravitational lensing and should average to zero, if only produced by intrinsic source orientations, and can therefore be used as an indication of systematic effects such as imperfect corrections for the point-spread function (Schneider 2003, and Appendix A.3).

The ESD is then estimated using the observed ellipticities of an ensemble of sources around the lens

$$\Delta\Sigma(R) = \langle \epsilon_+ \Sigma_{\text{cr,ls}} \rangle (R), \quad (18)$$

with each  $\epsilon_+ \Sigma_{\text{cr,ls}}$  an independent, albeit noisy estimate of the ESD. Here  $\langle \cdot \rangle$  denotes a weighted average, with weights to be specified.

$\Sigma_{\text{cr,ls}}$  behaves as a geometric scaling factor, indicating the lensing efficiency for each lens-source combination. Since the variance of the noise in  $\Delta\Sigma$  is then affected by  $\Sigma_{\text{cr,ls}}^2$ , the relative precision, or inverse variance, carried by each  $\epsilon_+$  scales as  $\Sigma_{\text{cr,ls}}^{-2}$ .

In this paper, we study the ESD profile in comoving radial bins, and we therefore use the comoving critical surface density

$$\Sigma_{\text{cr,com}} = (1 + z_l)^2 \Sigma_{\text{cr,prop}}. \quad (19)$$

In practice, the distance to each background source is not known exactly, and is estimated by its redshift probability distribution  $p(z_s)$ . Taking this into account, we estimate the comoving critical surface density via

$$\langle \Sigma_{\text{cr,ls}}^{-1} \rangle = \frac{4\pi G}{c^2} D(z_l) (1 + z_l)^2 \int \frac{D(z_l, z_s)}{D(z_s)} p(z_s) dz_s. \quad (20)$$

### 2.3. Statistical framework

In this section we discuss the estimation of  $\langle \epsilon_+ \Sigma_{\text{cr,ls}} \rangle$ , where we refer to paper I for a complementary discussion.

Important aspects of a good estimator  $\hat{e}$  are

- minimal bias, defined as the difference between the expected value of the estimator,  $\langle \hat{e} \rangle$ , and the value of the quantity being estimated, for instance the shear  $\gamma$ , or in this case  $\Delta\Sigma$ ;
- high efficiency, proportional to the inverse variance of the estimator,  $\sigma_{\hat{e}}^{-2}$ ;
- robustness, meaning the estimator retains these properties for a sufficient range of likely parameter distributions.

<sup>11</sup> Of the coordinate system in which  $\gamma_1$  and  $\gamma_2$  are defined.

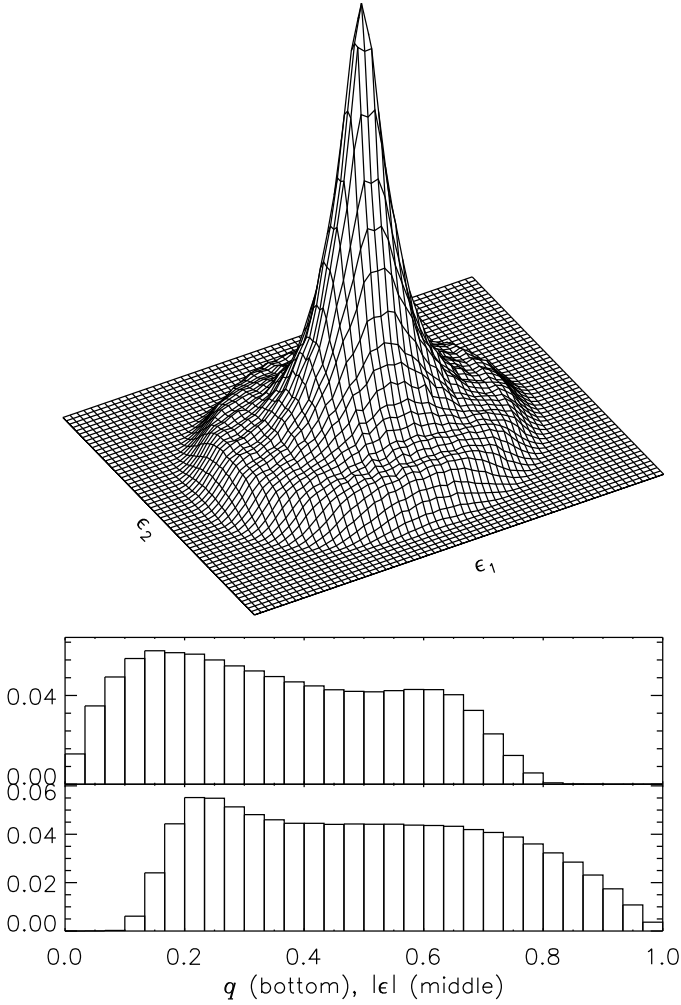


**Fig. 2.** Estimated ellipticity and axis ratio distributions of sources in the KiDS-450 catalog. Top: a 2D histogram of ellipticities. Middle: histogram of the absolute ellipticity  $|\epsilon|$ . Bottom: histogram of the ellipse axis ratio  $q$ .

### 2.3.1. Bias

Even though the measured ellipticity  $\epsilon$  is not a linear combination of the intrinsic shape  $\epsilon^I$  and the shear  $\gamma$ , it can be shown (Seitz & Schneider 1997) that, in the absence of further uncertainties, the mean  $\mu(\epsilon)$  is an unbiased estimator for the underlying shear, and that this is independent of the intrinsic ellipticity distribution  $P(\epsilon^I)$ .

In the canonical approach, the ESD is therefore estimated as a weighted mean of an ensemble of lens-source combinations

$$\Delta\Sigma(R) = \frac{\sum_{ls} w_{ls} \epsilon_{+,ls} \Sigma_{cr,ls}}{\sum_{ls} w_{ls}}, \quad (21)$$

where we use

$$w_{ls} = w_s \left\langle \Sigma_{cr,ls}^{-1} \right\rangle^2, \quad (22)$$

the weight  $w_s$  assigned to each measured ellipticity, scaled by the estimated lensing efficiency, as explained in the previous section (see e.g. Viola et al. 2015; Dvornik et al. 2017; Bellagamba et al. 2019).

In practice, there are various sources of uncertainty at each step of the process, such as source selection bias, distortion by

the point spread function (PSF) and biases due to the measurement pipeline. These lead to convolutions of the ellipticity distribution, before and after the gravitational lensing effect. The result is a bias in the mean as an estimate of the ESD (Melchior & Viola 2012; Refregier et al. 2012; Kacprzak et al. 2012; Viola et al. 2014; Kacprzak et al. 2014). In this case, the intrinsic shape distribution will play a role.

The weighted mean  $\mu$  is a statistic that, for a set of measurements  $\epsilon_i$  with weights  $w_i$ , finds the estimate  $\gamma$  that minimizes the loss function

$$S_\mu = \sum_i w_i \left[ (\epsilon_{i,1} - \gamma_1)^2 + (\epsilon_{i,2} - \gamma_2)^2 \right], \quad (23)$$

i.e. it is a least squares (LSQ) or  $L^2$  norm regression method and arises naturally as the optimal estimator for Gaussian distributions.

Figure 2 shows that the measured ellipticity distribution  $P(\epsilon)$  displays crucial differences with a Gaussian distribution, showing a sharp peak and a slower decline, including a higher number of high ellipticities  $|\epsilon|$ . This central peak is an unbiased tracer of the underlying shear (Paper I). By eq. 23, the mean is sensitive to outliers and therefore not robust when inferring the shear.

In contrast, the Least Absolute Deviation (LAD) or  $L^1$  norm regression minimizes the loss function

$$S_{LAD} = \sum_i w_i \sqrt{(\epsilon_{i,1} - \gamma_1)^2 + (\epsilon_{i,2} - \gamma_2)^2}. \quad (24)$$

The LAD estimate is also known as the median in one dimension or the spatial median in higher dimensions. LAD is more sensitive to the peak and less sensitive to high ellipticity outliers. Where the mean is expected to be biased low (Melchior & Viola 2012; Refregier et al. 2012; Kacprzak et al. 2012; Viola et al. 2014; Kacprzak et al. 2014), we expect this to be less for LAD (Paper I).

### 2.3.2. Efficiency

The formal definition of efficiency  $\tilde{\eta}$  relates the inherent (Fisher) information  $\mathcal{I}$  of a sample to the statistical variability around the expected value of the estimator, usually taken to be the variance  $\sigma_\epsilon^2$  of the estimator:

$$\tilde{\eta} = \frac{1}{\mathcal{I} \cdot \sigma_\epsilon^2}. \quad (25)$$

Since the variance of an unbiased estimator cannot be less than the reciprocal of the information,  $\mathcal{I}^{-1} \leq \sigma_\epsilon^2$ , we have  $0 \leq \tilde{\eta} \leq 1$  (Rao 1945; Cramer 1946).

As we are comparing two estimators with unknown bias, it is appropriate to use the relative efficiency

$$\eta = \frac{\sigma_\mu^2}{\sigma_{LAD}^2}, \quad (26)$$

with  $\eta < 1$  indicating a higher efficiency for the mean, and vice versa.

Paper I showed LAD performed consistently better than the mean, with both higher efficiency and less bias, for various cusped intrinsic ellipticity distributions, including the shear catalog from CFHTLenS. In what follows we will take the CFHTLenS shear distribution shape to be representative of KiDS data as well, since both surveys were processed with the THELI-pipeline (Erben et al. 2013) and the shape measurement pipeline *lensfit* (Miller et al. 2007; Kitching et al. 2008; Miller et al. 2013).

## 2.4. Halo model

Studying the effects of estimator choice on the weak lensing signal forms the technical core of this paper. The scientific goal, however, is to assess the relevance on the inference of physical quantities, such as the derivation of a lensing halo mass from an ESD profile. Since we calculate the stacked signal for an ensemble of clusters with some common (observable) property (here a range in  $r$ -band luminosity) of interest is the scaling relation between observable and derived lensing mass  $M_{200}$ , where we use the definition with respect to the mean density of the universe.

To do so, we model the lens density profile the same way as Dvornik et al. (2017), using the halo model (Seljak 2000; Peacock & Smith 2000; Cooray & Sheth 2002; van den Bosch et al. 2013; Cacciato et al. 2013; Mead et al. 2015).

The initial lens density profile is described by a Navarro-Frenk-White profile (Navarro et al. 1995, hereafter NFW). We use the mass-concentration relation given by Duffy et al. (2008) and allow for a renormalization factor  $f_c$  (Viola et al. 2015).

A dominant source of systematic bias in stacked weak lensing analyses is a miscentering of the lenses, which can be due to an offset of the cluster halo with the visible distribution of galaxies (see e.g. George et al. 2012) or the resolution of the cluster detection method (less than  $0.1 \text{ Mpc } h^{-1}$  for AMICO, see Bellagamba et al. 2018). Following Johnston et al. (2007) as well as numerous subsequent works (e.g. Oguri et al. 2010; Viola et al. 2015; Dvornik et al. 2017; Bellagamba et al. 2019; Giocoli et al. 2021), we allow a fraction  $p_{\text{off}}$  of clusters to be offset from the center of the galaxy distribution, effectively smoothing the central stacked  $\Delta\Sigma$  profile with a characteristic radius  $R_{\text{off}}$ .

At large radii, typically beyond a few Mpc, the clustering of dark matter halos starts to dominate the signal. This ‘two-halo’ term depends on the halo bias  $b$  (Dvornik et al. 2017) and is modeled following Tinker et al. (2010).

At small radii, the baryonic component of central galaxies can contribute to the signal, which is adequately described by a point mass  $M_\star$  in the model (Viola et al. 2015; Dvornik et al. 2017).

In Table 1 we summarize these six free parameters for our halo model implementation, analogous to Dvornik et al. (2017).

**Table 1.** Summary of the halo model fitting parameters and priors.

Parameter	Prior
$f_c$	[0.0, 8.0]
$p_{\text{off}}$	[0.0, 1.0]
$R_{\text{off}}$ [ $h^{-1} \text{ Mpc}$ ]	[0.0, 1.0]
$b$	[0.0, 10.0]
$\log(M_\star)$ [ $\log[ h^{-1} M_\odot ]$ ]	[9.5, 12.5]
$\log(M_{200})$ [ $\log[ h^{-1} M_\odot ]$ ]	[11.0, 17.0]

In the AMICO cluster sample with 6925 lenses in 440 square degrees, many background sources are lensed by more than one cluster, contributing to the estimate of the ESD profile in various radial bins of different clusters. In the model fitting we take into account the covariance between the ESD estimates, as described in Section 3.3.2 (Viola et al. 2015; Dvornik et al. 2017; Bellagamba et al. 2019).

## 3. Data and analysis

In this paper we use a lensing cluster catalog and background source catalog from the KiDS Data Release 3 (KiDS-450, de Jong et al. 2017), an optical wide-field imaging survey with OmegaCAM (Kuijken 2011) on the VLT Survey Telescope (VST Capaccioli & Schipani 2011; de Jong et al. 2013).

KiDS-450 consists of two patches, KiDS-N and KiDS-S (see Fig. 3), with 454 tiles of imaging data, for a total of  $449.7 \text{ deg}^2$ , in four optical filters  $ugri$ . The survey was designed for lensing, ensuring a stable point spread function (PSF), low seeing ( $< 0.96''$ , with an average of  $0.66''$  in  $r$ ) and good photometric redshifts (photo- $z$ , Hildebrandt et al. 2017).

The KiDS data are reduced with ASTRO-WISE (Valentijn et al. 2007; Verdoes Kleijn et al. 2012; Begeman et al. 2013; McFarland et al. 2013), as described in de Jong et al. (2015); Hildebrandt et al. (2017). Photo- $z$ ’s, also termed  $z_B$ , were determined using a Bayesian photo- $z$  estimation (BPZ, Benítez 2000; Coe et al. 2006) with PSF-matched photometry, as described in Hildebrandt et al. (2012); Kuijken et al. (2015); Hildebrandt et al. (2017).

### 3.1. Lenses

We make use of the galaxy cluster catalog derived with the Adaptive Matched Identifier of Clustered Objects (AMICO) (Bellagamba et al. 2011; Radovich et al. 2017; Bellagamba et al. 2018), extracted from 440 tiles of KiDS-450 data, described in Maturi et al. (2019) and Bellagamba et al. (2019).

For each cluster, the luminosity  $L_{200}$  is defined<sup>12</sup> as the sum of  $r$ -band luminosities of bright candidate member galaxies, weighted by membership probability (see Maturi et al. 2019). We select galaxies with  $k$ -corrected  $r$ -band magnitudes brighter than  $m^*(z_1) + 1$  within  $R_{200}(z_1)$ , where  $z_1$  is the estimated cluster redshift and  $R_{200}$  is derived from the adopted cluster model and used in the construction of the cluster detection filter, as defined in Maturi et al. (2019). In this sense,  $L_{200}$  is defined analogously to the apparent richness  $\lambda^*$ , which is a sum of membership probabilities of galaxies with  $m < m^* + 1.5$ , within  $R_{200}$ .

We select clusters in the range  $0.1 \leq z_1 \leq 0.6$ . We exclude clusters below  $z = 0.1$  due to their unfavorable lensing geometry and above  $z = 0.6$  due to the low density of background sources. For some clusters no lens-source pairs were found due to source selection criteria or masking. Our final selection comprises 6925 clusters, divided over the KiDS-450 survey area as shown in Fig 3 and described in Table 2. The redshift distribution of these clusters is shown in Fig. 4, with a median redshift of  $z_1 = 0.39$ .

**Table 2.** Summary of the survey patches<sup>1</sup>, with corresponding numbers of KiDS mosaic tiles and analyzed clusters.

KiDS field	Subfield	Tiles	Clusters
North	G9	65	1039
	G12	113	1778
	G15	112	1737
South	G23	101	1517
	GS	63	854

**Notes.** <sup>(1)</sup> as described in Hildebrandt et al. (2017)

<sup>12</sup> We note that this does not take into account intracluster light.

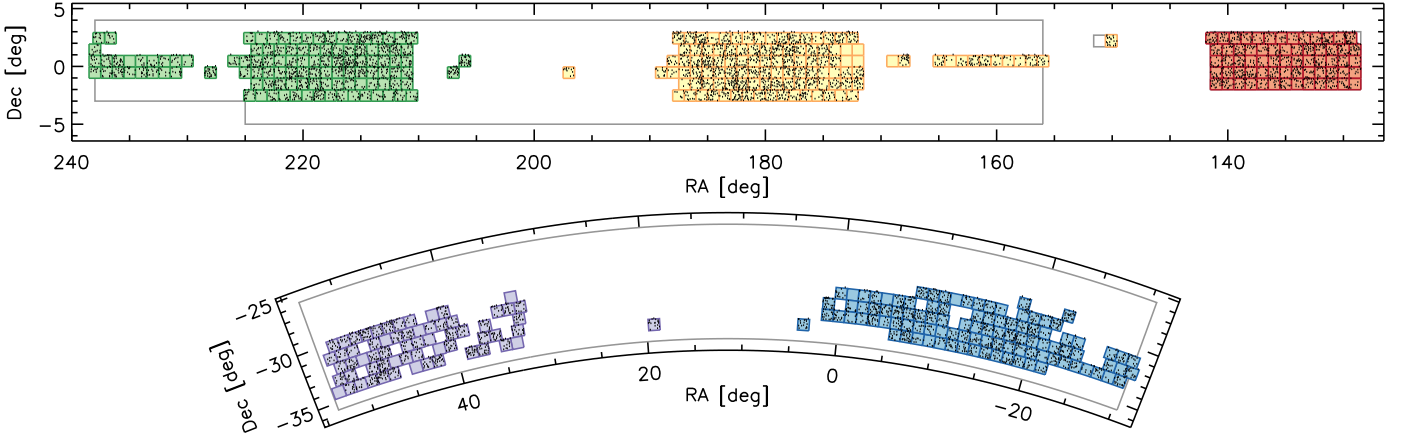


**Fig. 3.** Overview of the KiDS-450 observations, with the KiDS-N (upper) and KiDS-S (lower) patches. The solid gray lines represent the planned KiDS survey area. Overplotted are the observed 1 sq. degree tiles, color-coded with respect to their correspondence with the GAMA survey patches (G9 red, G12 yellow, G15 green, G23 blue, and GS purple; see Hildebrandt et al. 2017, for more details). The AMICO clusters analyzed in this work are represented by black dots.

We divide the clusters in 13 bins of cluster  $L_{200}$ . The limits of these bins are chosen so, that the signal-to-noise ratios of the ESD measurements are approximately the same in each bin. We give an overview of these bins, together with the estimated  $M_{200}$ , in Table 3.

### 3.2. Sources

We select an initial sample of background sources, using the same photometric redshift criteria as Hildebrandt et al. (2017),  $0.1 < z_B \leq 0.9$ , to reduce the outlier rate. We also apply the cut  $z_1 + \Delta z < z_B$ , following Dvornik et al. (2017). Here  $\Delta z = 0.2$  is an offset between the redshift estimation  $z_1$  of the cluster by AMICO and the photometric redshift  $z_B$  of the source to sufficiently lessen the contamination of the background sample by cluster member galaxies (see also appendix A.2).

Our selection of AMICO clusters is deeper than the lenses from the GAMA catalog used in Dvornik et al. (2017). As can be seen in Fig. 4, the redshift distributions of lenses and background sources significantly overlap and the cut at  $\Delta z = 0.2$  reduces the number density severely for clusters at higher redshift. Following Bellagamba et al. (2019), we also select background sources using the color selection proposed by Oguri et al. (2012):

$$g - r < 0.3 \quad \vee \quad r - i > 1.3 \quad \vee \quad r - i > g - r. \quad (27)$$

In Fig. 5, we show the photometric redshift distribution of this cut in the KiDS-450 catalog, and compare it to the photometric and spectroscopic redshift distribution of the same cut in the spectroscopic redshift (spec- $z$ ) catalog used in Hildebrandt et al. (2017). Based on this analysis, we additionally require  $z_B \geq 0.6$  for this selection, to reduce contamination by sources at low redshift and find that 98 % of the galaxies in this color selection has  $z_{\text{spec}} > 0.6$ .

#### 3.2.1. Redshift distribution

To estimate the redshift distribution of background galaxies, we do not directly use the individual redshift probability distribution  $p(z_s)$  per source galaxy, but apply a weighted direct calibration method (DIR), as motivated by Hildebrandt et al. (2017).

For each cluster, we use the spec- $z$  catalog described in Hildebrandt et al. (2017) to select objects using the same selection criteria as described above. We then use the normalized

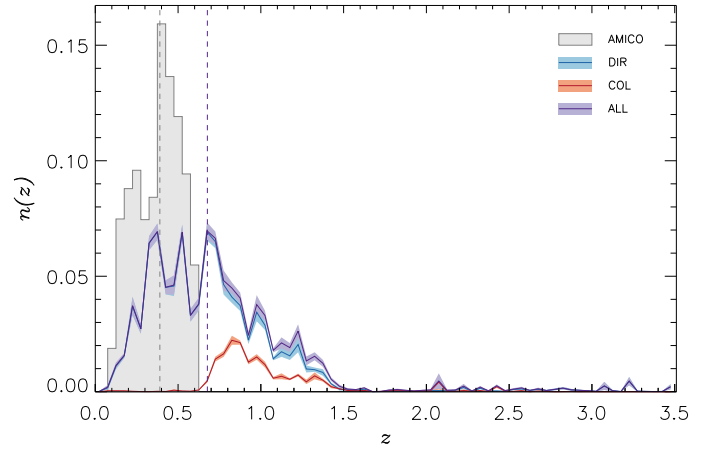


**Fig. 4.** Redshift distribution of AMICO clusters (gray), with a median redshift of  $z_1 = 0.38$  (dashed gray), and KiDS-450 background sources (purple), with a median redshift of  $z = 0.68$  (dashed purple). In blue (DIR), we show the initial selection following Hildebrandt et al. (2017); Dvornik et al. (2017). In red, we show the estimated redshift distribution of the  $gri$  color selection (COL), corresponding to the bottom panel of Fig. 5.

spectroscopic redshift distribution  $n(z_s)$  of this sample to calculate the comoving critical surface density analogous to Eq. 20:

$$\langle \Sigma_{\text{cr},1}^{-1} \rangle = \frac{4\pi G}{c^2} D(z_1) (1 + z_1)^2 \int_{z_1 + \Delta z}^{\infty} \frac{D(z_1, z_s)}{D(z_s)} n(z_s) dz_s. \quad (28)$$

The resulting redshift distribution for selected sources from the full KiDS-450 catalog is shown in Figure 4.

#### 3.2.2. Shape measurements

For shape measurements, the  $r$ -band data are reduced using the THELI-pipeline, developed to meet the requirements for weak gravitational lensing analyses (Erben et al. 2005, 2009; Schirmer 2013; Erben et al. 2013).

Galaxy shapes in the KiDS-450 catalog are then measured by *lensfit* (Miller et al. 2007; Kitching et al. 2008; Miller et al. 2013; Fenech Conti et al. 2017).



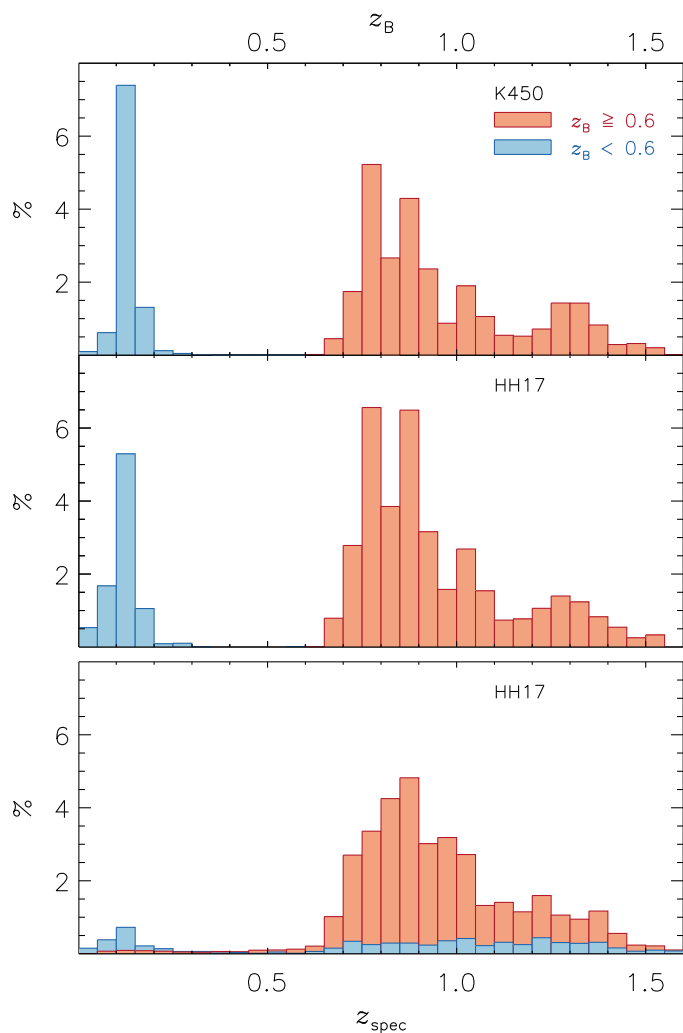


**Fig. 5.** Redshift distribution of background sources selected by color. The upper panel shows the distribution of the photometric redshift  $z_B$  of the sources in the KiDS-450 catalog satisfying the color cut of Eq. 27, of which we select the sources with  $z_B \geq 0.6$  (red) and discard those with  $z_B < 0.6$  (blue). The bottom two panels show the same selection applied to the spec- $z$  catalog (Hildebrandt et al. 2017), plotted in terms of photometric (middle) and spectroscopic redshift (lower). We find the contamination of sources with  $z_B \geq 0.6$  and  $z_{\text{spec}} < 0.6$  is  $\sim 2\%$ .

For each source, *lensfit* produces the ellipticity ( $\epsilon_1, \epsilon_2$ ), an approximately inverse-variance weight  $w_s$  (see Miller et al. 2013), and a fitting quality parameter. We exclude sources with unreliable ellipticities from our source sample, using the same *lensfit* selection criteria as described in Hildebrandt et al. (2017).

In Paper I, we compared the performance of estimators for ellipticity measurements in the CFHTLenS data with a subset of that catalog, selecting sources on the signal-to-noise ratio parameter  $\nu_{\text{SN}}$  output by *lensfit*. We repeat that approach for a qualitative comparison here, using two subsets of the selected KiDS-450 sources. The first set selects sources with  $\nu_{\text{SN}} \geq 20$ , similar to paper I, retaining  $\sim 30\%$  of the full background sample. The second set is a more stringent cut of the first set, additionally selecting objects with  $w_s \geq 14.5$ , comprising  $\sim 20\%$  of the full sample.

### 3.2.3. Effective source density

The KiDS-450 catalog includes a filtering on general object detection and quality flags, e.g. possibly blended sources or artifacts, as described by Kuijken et al. (2015); Hildebrandt et al. (2017), and we discard objects that lie in a mask, which removes approximately  $\sim 12\%$  of the sources.

Our final selection comprises 14124197 sources, which translates to an effective number density of  $n_{\text{eff}} \approx 8.23 \text{ arcmin}^{-2}$ , as defined in Heymans et al. (2012):

$$n_{\text{eff}} = \frac{1}{A} \frac{(\sum_i w_i)^2}{\sum_i w_i^2}, \quad (29)$$

with  $A$  the effective surface area, excluding masked regions.

## 3.3. Implementation

### 3.3.1. ESD estimation

Following Bellagamba et al. (2019), we measure the ESD in 14 logarithmic bins between  $0.1 \text{ Mpc } h^{-1}$  and  $3.16 \text{ Mpc } h^{-1}$ . Not only does this make for an easy comparison of the results, but it has several practical advantages.

We avoid radii smaller than the AMICO detection pixel size, which has a median size of  $0.1 \text{ Mpc } h^{-1}$ , to lessen the chance of a mismodeling of the halo miscentering (Section 2.4). Here, the line of sight is also most contaminated by cluster members, which can lead to an overabundance by incorrectly including ellipticity measurements that carry no lensing signal, or obscuring and blending of background sources, which leads to an underabundance of sources. While these effects may partially cancel out in the number counts, the effects on the ESD measurements do not cancel out, as the first leads to a diluted signal and the second to a very poor signal-to-noise ratio. See Appendix A.2 for an assessment of cluster member contamination.

At large radii, systematic additive biases can start to play a role (see e.g. Dvornik et al. 2017, for this dataset), which may differ for each KiDS survey patch (Fenech Conti et al. 2017; Hildebrandt et al. 2017). As another concern at larger separations, the two-halo term becomes the dominant contribution to the ESD signal, which means we would need to properly constrain the halo bias, and we explain below how our approach does not fully take the clustering of dark matter halos into account.

The combination of background selection criteria from Dvornik et al. (2017) and Bellagamba et al. (2019) allows us to retain the three inner radial bins between  $0.1$  and  $0.2 \text{ Mpc } h^{-1}$ . We justify this inclusion in Appendix A.2, where we repeat the tests of Dvornik et al. (2017).

Each lens-source pair is then assigned a combined weight of

$$w_{\text{ls}} = w_s \Sigma_{\text{cr},1}^{-2}, \quad (30)$$

as motivated in section 2.2.

For LAD optimization, the estimator that minimizes the  $L^1$  norm (eq. 24), there exists no general analytic solution. The problem can however be formulated as a linear optimization, which can be solved iteratively (e.g. simplex-based methods, Barrodale & Roberts 1973). In our weak lensing analyses, we find that convergence is robust.

To derive the covariance matrices for the ESD estimates using the mean and LAD in the same way, we can therefore also not employ the analytical prescription of Viola et al. (2015) used in earlier KiDS analyses (e.g. Sifón et al. 2015; van Uitert et al.



2016; Brouwer et al. 2016). Instead, we use a bootstrap approach.

Since the cluster bins of highest  $r$ -band luminosity  $L_{200}$  contain only a small number of clusters, covering only a small fraction of the KiDS-450 tiles, we cannot use the same bootstrap approach as Viola et al. (2015); Dvornik et al. (2017) by bootstrapping 1 deg<sup>2</sup> tiles with replacement. Instead, we bootstrap the source catalog, in accordance with Bellagamba et al. (2019).

This means we are not sensitive to the clustering effect of dark matter halos, which justifies our choice of radial lens-source separation mentioned above. To assess the accuracy of these assumptions, we estimate the covariance matrix of the full 6925 cluster sample by bootstrapping the sources and by bootstrapping by KiDS-450 tiles in Appendix A.4. We conclude that our bootstrapping method yields a good estimate of the covariance matrix.

### 3.3.2. Halo model fitting

Having produced the LSQ and LAD shear profiles for the stacked clusters, we fit a halo model to the results. We use the fitting procedure described in Dvornik et al. (2017), producing the full posterior probabilities by a Bayesian inference technique, via a Monte Carlo Markov Chain (MCMC) maximum likelihood approach. We assume a Gaussian likelihood and make use of the full covariance between radial bins:

$$\mathcal{L} \propto \exp \left[ -\frac{1}{2} \mathbf{R}^T \mathbf{C}^{-1} \mathbf{R} \right], \quad (31)$$

where  $\mathbf{R}$  are the residuals and  $\mathbf{C}$  is the covariance matrix.

We use the `emcee` Python package (Foreman-Mackey et al. 2013) for the MCMC procedure, setting flat priors for all parameters. For the evaluation of the power spectrum and the halo mass function, we use the median redshift for each cluster luminosity bin.

## 4. Results

We present our results, starting with the derived ESD profiles obtained with the mean and LAD estimators, discussing potential biases and efficiency. Then, we show the results of the halo model fitting, i.e.  $M_{200}$  for each luminosity bin, and conclude with the scaling relation between  $L_{200}$  and  $M_{200}$ .

We visualize the results for the case all 6925 clusters are stacked together, giving the numerical results of the 13 luminosity bins in Table 3.

### 4.1. ESD profiles

We calculated the ESD profiles using 10<sup>4</sup> bootstraps with replacement. We estimated the ESD signal in the 14 radial bins, using both the mean and the LAD estimators, for each bootstrapped sample, preserving the bootstrap order of all 28 values throughout the whole process.

We find the estimator distribution to be almost perfectly normal, as is expected by the central limit theorem. The correlation between the 14 bins of the full stack of clusters is shown in Fig. 6, given by

$$\rho_{ij} \equiv \frac{\text{Cov}_{ij}}{\sigma_i \sigma_j}, \quad (32)$$

where  $i$  and  $j$  denote the radial bin subscripts.

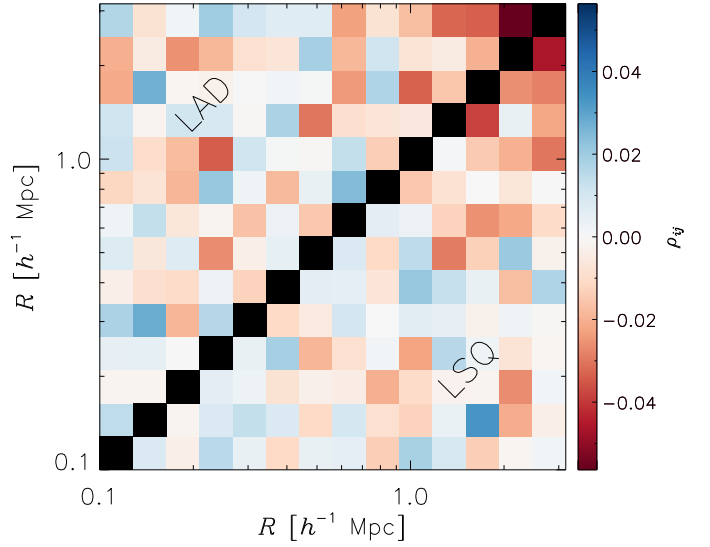


**Fig. 6.** Correlation matrix between the stacked ESD signals in different radial bins, using the full AMICO cluster catalog and 10<sup>4</sup> bootstraps. The upper left triangle shows the correlation  $\rho_{\text{LAD}}$  between the LAD estimations. The lower right triangle shows the correlation  $\rho_{\text{mean}}$  between the ESD estimates using a weighted mean. We note the general similarities in the two patterns.

The upper left part of the matrix shows the correlation between the LAD estimates of the radial bins and the lower right part shows the mean results. Although the correlation between bins is very low, it is clear that the overall trends are the same for the two estimators.

The signal-to-noise ratio of the recovered ESD profile of the full stack, which is shown in Fig. 7, is high enough to notice the difference between the estimators, indicating a small relative bias. The blue points show the LAD estimates, while the red points represent the mean estimates, with error bars in both cases defined as the square root of the diagonal elements of the covariance matrices, i.e. the classical standard deviation.

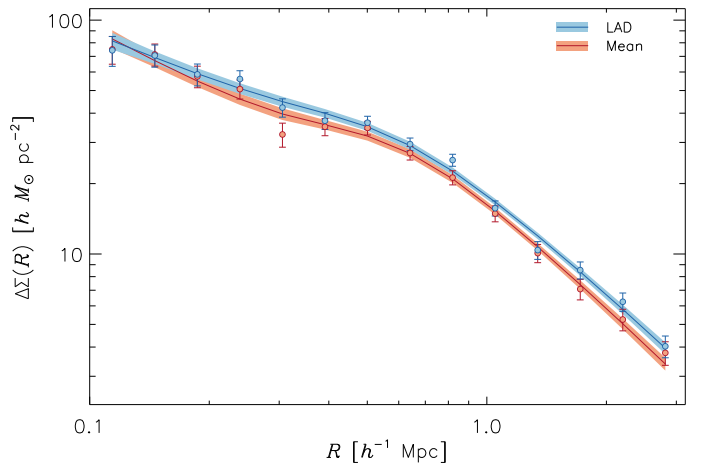


**Fig. 7.** Estimated ESD profile from the full AMICO cluster catalog, using the LAD estimator (blue) and a weighted mean (red). The error bars are the square roots of the diagonal values of the respective covariance matrices. The solid lines represent the best-fitting halo model obtained by the MCMC fit. The shaded regions show the 68.3% confidence bands, estimated using the 15.9th and 84.1th percentiles of the MCMC realizations.

Tests for systematic effects, such as the cross signal and a test for systematic additive noise around random points, were already conducted by Dvornik et al. (2017) and Bellagamba et al. (2019). In Appendix A we reiterate these tests for completeness, since we use the KiDS-S field and an extended source selection with respect to Dvornik et al. (2017) and used a different source selection and three smaller radial bins with respect to Bellagamba et al. (2019). Our results show no residual systematic effects, in accordance with these papers.

#### 4.2. Bias and efficiency

A possible bias is expected to depend on the strength of the underlying shear field, as a zero lensing signal would imply no bias. In that case, the expected relevant distributions, tangential ellipticities or noise, are symmetric around zero ellipticity.

To quantify the difference between the ESD estimates, which we call the relative bias  $\Delta\Sigma_{\text{Mean}} - \Delta\Sigma_{\text{LAD}}$ , we assume<sup>13</sup> to first order

$$\Delta\Sigma_{\text{Mean}} - \Delta\Sigma_{\text{LAD}} = m \cdot \Delta\Sigma, \quad (33)$$

where we arbitrarily<sup>14</sup> use  $\Sigma_{\text{LAD}}$  for  $\Sigma$ .

We use the full stack for its high signal-to-noise ratio, using the 15.9th and 84.1th percentiles of the differences in all bootstrap results to calculate uncertainties for each bin. We find  $m = -0.088 \pm 0.020$ . In Fig. 8, we show this relative bias, plotting for visualization purposes

$$\frac{\Delta\Sigma_{\text{Mean}} - \Delta\Sigma_{\text{LAD}}}{\Delta\Sigma} \quad (34)$$

and a horizontal line at  $m = -0.88$ , to give a more intuitive impression of the relative error bars.

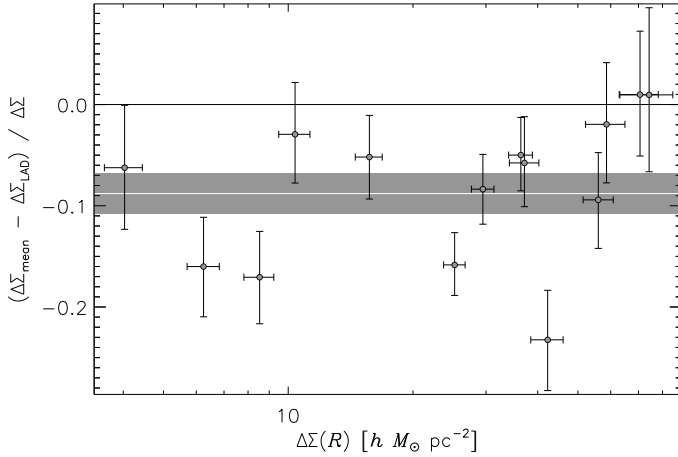


**Fig. 8.** Difference between the recovered ESD signals in the radial bins, showing  $(\Delta\Sigma_{\text{mean}} - \Delta\Sigma_{\text{LAD}}) / \Delta\Sigma$ . The solid white line represents the average difference, with the shaded region showing the formal  $1\sigma$  error. As a possible bias in the recovered values is expected to increase with increasing shear, the differences are plotted versus the full ESD signal in each bin, where we use  $\Delta\Sigma_{\text{LAD}}$ , but we note that the small variations in the individual points, when plotting against  $\Delta\Sigma_{\text{mean}}$  instead, give the same result, within statistical significance.

We reiterate that it is impossible to determine the absolute bias of each estimator, as we have no knowledge of the true ESD,

<sup>13</sup> This assumption is only made here, to quantify the bias, and is not used elsewhere in the paper

<sup>14</sup> We find no qualitative difference in our results, when we use  $\Delta\Sigma_{\text{Mean}}$  instead.

as we did in Paper I. However, the overall trend between the mean and LAD is similar in sign and order of magnitude, as we found for the CFHTLenS data in Paper I.

In Fig. 9, we show the derived relative efficiency (Eq. 26)  $\eta = 1.047 \pm 0.006$ , which is in accordance with the findings for CFHTLenS data in Paper I.

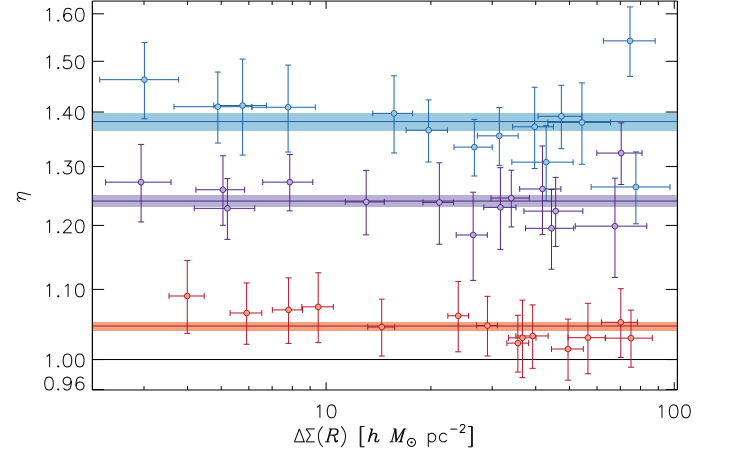


**Fig. 9.** Relative efficiencies  $\eta \equiv \sigma_{\text{Mean}}^2 / \sigma_{\text{LAD}}^2$ , defined as the ratio of the diagonal elements of the covariance matrices. The relative efficiencies using the full KiDS-450 source catalog are shown in red. The purple and blue represent the higher S/N and higher *lensfit* weight selections, respectively. The solid lines represent the average  $\eta$  for each selection, with the shaded regions showing the  $1\sigma$  errors.

The measured<sup>15</sup> ellipticity distribution is expected to differ for shape measurements with a higher signal-to-noise ratio. For example, the cuspsiness of the distribution shown in Fig. 2 above can be smoothed out by noise convolutions. As the LAD estimation is more sensitive to the central peak, this will affect its precision.

In paper I, this was confirmed in the comparison of simulated data with and without noise, and in the results of the CFHTLenS sample with a stringent signal-to-noise selection compared with the full sample. As in Paper I, we compare the relative efficiencies for our selections with  $v_{\text{SN}} \geq 20$  and with  $w_i \geq 14.5$ , finding indeed a higher efficiency for less noisy shapes, namely  $\eta = 1.240 \pm 0.010$  and  $\eta = 1.386 \pm 0.018$ , respectively.

#### 4.3. Halo masses

We run MCMC chains of 120 000 samples, using 120 walkers with 1000 steps each. The resulting chains are fully converged after the first 200 steps, so we discard the first 24 000 samples.

We summarize the  $M_{200}$  derived from the ESD estimation of the 13 luminosity bins in Table 3. Reduced  $\chi^2$ , estimated between 0.730 and 2.528, are fairly consistent between derived results for mean and LAD.

For the full stack of clusters, we derive

$$M_{200} = (0.453^{+0.030}_{-0.030}) \times 10^{14} h^{-1} M_{\odot}, \quad \chi^2_{\nu} = 1.25 \quad (\text{Mean}) \quad (35a)$$

$$M_{200} = (0.487^{+0.033}_{-0.036}) \times 10^{14} h^{-1} M_{\odot}, \quad \chi^2_{\nu} = 1.37 \quad (\text{LAD}) \quad (35b)$$

<sup>15</sup> i.e. the combination of the intrinsic distribution and the various effects before and after the lensing by AMICO clusters, that affect the observation and measurement of the source ellipticities.

**Table 3.** Properties and lensing results of the individual luminosity bins.

Luminosity bin	Median $L_{200}$	Clusters	Median $z_1$	$M_{200}$ Mean	$\chi^2_\nu$	$M_{200}$ LAD	$\chi^2_\nu$
$[10^{10} h^{-2} L_\odot]$	$[10^{10} h^{-2} L_\odot]$			$[10^{14} h^{-1} M_\odot]$		$[10^{14} h^{-1} M_\odot]$	
[0.4, 17.4[	$12.3^{+3.5}_{-4.6}$	2346	0.29	$0.187^{+0.029}_{-0.026}$	1.27	$0.191^{+0.031}_{-0.026}$	1.18
[17.4, 24.8[	$20.8^{+2.7}_{-2.3}$	1545	0.41	$0.416^{+0.061}_{-0.076}$	2.19	$0.445^{+0.055}_{-0.061}$	1.60
[24.8, 31.8[	$28.0^{+2.5}_{-2.2}$	1027	0.41	$0.371^{+0.048}_{-0.046}$	0.81	$0.385^{+0.050}_{-0.046}$	0.91
[31.8, 40.5[	$35.2^{+3.2}_{-2.4}$	685	0.42	$0.519^{+0.078}_{-0.078}$	1.34	$0.621^{+0.076}_{-0.074}$	1.29
[40.5, 49.0[	$44.4^{+2.9}_{-2.7}$	457	0.42	$1.076^{+0.182}_{-0.181}$	2.18	$0.998^{+0.150}_{-0.139}$	2.53
[49.0, 59.9[	$54.1^{+3.6}_{-3.9}$	305	0.40	$1.387^{+0.425}_{-0.335}$	1.05	$1.462^{+0.533}_{-0.353}$	0.98
[59.9, 72.9[	$65.2^{+5.2}_{-3.7}$	202	0.41	$1.318^{+0.267}_{-0.234}$	0.77	$1.309^{+0.233}_{-0.203}$	0.74
[72.9, 84.1[	$78.6^{+3.2}_{-3.9}$	135	0.38	$1.406^{+0.344}_{-0.215}$	1.22	$1.528^{+0.409}_{-0.254}$	1.30
[84.1, 102[	$91.8^{+5.7}_{-4.8}$	90	0.39	$2.438^{+0.486}_{-0.443}$	0.75	$2.472^{+0.479}_{-0.425}$	0.73
[102, 129[	$112^{+10}_{-7.2}$	60	0.40	$2.143^{+0.618}_{-0.417}$	0.77	$1.914^{+0.680}_{-0.373}$	0.79
[129, 160[	$138^{+11}_{-6.9}$	40	0.395	$3.999^{+1.957}_{-0.993}$	1.35	$3.715^{+1.557}_{-0.910}$	1.64
[160, 221[	$175^{+27}_{-11}$	26	0.37	$4.207^{+0.713}_{-0.610}$	1.47	$4.786^{+0.824}_{-0.637}$	1.18
[221, 400[	$277^{+106}_{-24}$	8	0.375	$7.638^{+2.293}_{-1.613}$	1.02	$9.141^{+3.105}_{-1.913}$	0.81

**Notes.** The errors on the median  $L_{200}$  and derived  $M_{200}$  in each luminosity bin are the differences with the 15.9th and 84.1th percentiles.

where the confidence intervals are derived from the 15.9th and 84.1th percentiles of the posterior distributions.

The best fitting ESD models are shown in Fig. 7. The 68.3% confidence bands overlap at some radii and are in tension at other radii. While the difference in ESD is significant, the 68.3% confidence intervals for  $M_{200}$  just touch.

#### 4.4. $L_{200} - M_{200}$ scaling relation

We assume a power-law relation between the derived halo masses and the median  $r$ -band luminosity of each cluster bin. We fit this relation in the form

$$\log\left(\frac{M_{200}}{M_{\text{piv}}}\right) = a + b \log\left(\frac{L_{200}}{L_{\text{piv}}}\right), \quad (36)$$

with  $a$  the intercept and  $b$  the slope, where  $M_{\text{piv}} \approx 10^{14.1} h^{-1} M_\odot$  and  $L_{\text{piv}} \approx 10^{11.8} h^{-2} L_\odot$  are typical pivotal values of the halo mass and luminosity, derived from the fit itself. The fit is done in log-basis, as the derived posterior distributions of the halo mass are log-normal.

We do not take a redshift dependence into account, as Belagamba et al. (2019) showed only a marginal and not very steep dependence of the halo mass on redshift.

We obtain the scaling relations

$$\frac{M_{200}}{10^{14.1} h^{-1} M_\odot} = (0.97 \pm 0.06) \left( \frac{L_{200}}{10^{11.8} h^{-2} L_\odot} \right)^{(1.24 \pm 0.08)} \quad (\text{Mean}) \quad (37a)$$

$$\frac{M_{200}}{10^{14.1} h^{-1} M_\odot} = (1.03 \pm 0.05) \left( \frac{L_{200}}{10^{11.8} h^{-2} L_\odot} \right)^{(1.24 \pm 0.08)} \quad (\text{LAD}) \quad (37b)$$

and plot the results in Fig. 10. Like the derived ESD profiles and halo masses for the full stack of clusters, the 68.3% confidence bands just touch at the pivot point

$$(L_{200}, M_{200}) = (10^{11.8} h^{-2} L_\odot, 10^{14.1} h^{-1} M_\odot), \quad (38)$$

recognizable as the narrowest parts of the confidence bands.

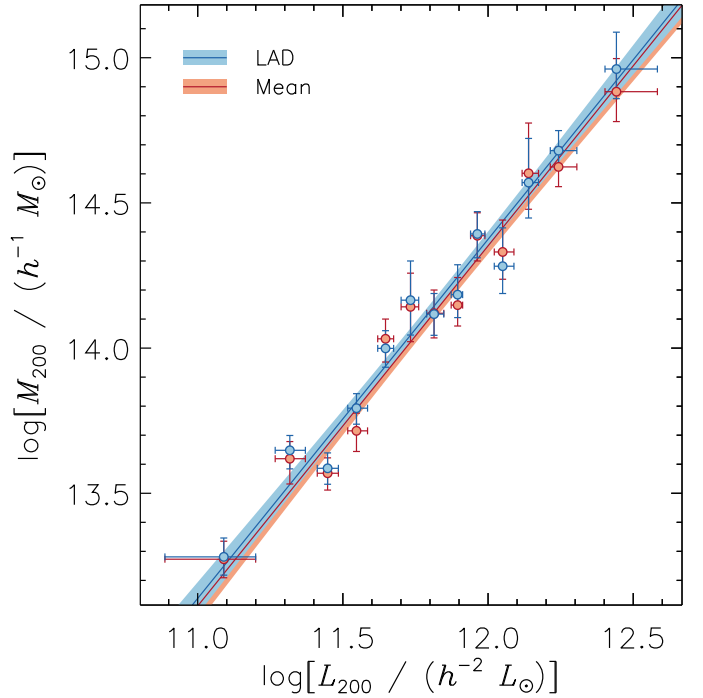


**Fig. 10.** The  $r$ -band luminosity-halo mass scaling relations, derived from the ESD profiles estimated using the weighted mean (red) and LAD (blue). At the pivot point, recognizable as the narrowest parts of the confidence bands, the relations just touch at the 68.3% confidence level.

## 5. Summary and conclusions

We conducted a weak shear analysis of 6925 AMICO clusters in the KiDS-450 data, deriving a tightly constrained scaling relation between  $r$ -band luminosity  $L_{200}$  and derived average lensing masses  $M_{200}$ , in concordance with earlier results in the literature.

We investigated the impact of estimator choice for inferring the central moment of the cusped and skewed ellipticity distribu-

tion of background galaxies, finding a relative bias of the order of a few percent, as predicted in Paper I. We find the constraints obtained via LAD regression tighter than those obtained via LSQ regression, and significantly improving with signal-to-noise ratio of the shape measurements of the background galaxies. Complemented by simulations from Paper I, we give an alternative perspective on the problem of inferring the central shear value from the skewed distribution of background galaxy shapes, at the minor cost of increased, but still feasible computation times for numerical, iterative regression.

### 5.1. $L_{200} - M_{200}$ relation

Since the relative bias we found, in this research and in Paper I, is approximately proportional to the ESD signal, it is expected that the LAD estimator will mainly have an effect on the intercept of the  $L_{200} - M_{200}$  scaling relation, as we concluded in Equation 37.

The power-law index of the  $L_{200} - M_{200}$  scaling relation was constrained to  $1.24 \pm 0.08$  (Eq. 37), independent of estimator choice. This is in agreement with earlier literature, such as Viola et al. (2015, and references therein), who cite  $1.16 \pm 0.13$ . This agreement is noteworthy, since the AMICO clusters are derived from photo- $z$ 's as opposed to the spectroscopically derived groups from GAMA (Driver et al. 2011; Robotham et al. 2011). The difference in confidence is explained by the increased number of lenses, not surprising given the large overlap in mass range: Viola et al. (2015) analyzed 1413 galaxy groups between  $z = 0.03$  and  $z = 0.33$ , with  $r$ -band luminosity bin limits between  $2.5 \times 10^9$  and  $5.0 \times 10^{12} h^{-2} L_{\odot}$ , deriving halo masses between  $1.4 \times 10^{13}$  and  $3.5 \times 10^{14} h^{-1} M_{\odot}$ .

The choice of estimator produces a difference in intercept at just the  $1\sigma$  level. Using a weighted mean to derive the ESD leads to an intercept of  $0.97 \pm 0.06$  in the scaling relation, while LAD gives an intercept of  $1.03 \pm 0.05$ . This is to be expected, as the relative bias seems roughly constant, when normalized by the ESD (see Fig. 8), and in good agreement with the bias of  $\sim 5\%$  found using simulations in Paper I.

As in Bellagamba et al. (2019), we estimate that systematic effects mostly affect the intercept. While the derived intercept is in agreement with aforementioned literature, we note that the chosen definition<sup>16</sup> of  $L_{200}$  and the difference in redshift range and definitions and completeness of group and cluster membership, can account for possible differences of the same order of magnitude. This would not affect our conclusions on methodology, as the results from both estimators would be similarly affected.

In further comparison with the scaling relation between richness and mass, cited in Bellagamba et al. (2019), we find similar significance in constraints on the slope. We define bins in luminosity instead of AMICO detection amplitude (Radovich et al. 2017) or richness, but since the cluster luminosity is tightly correlated with the richness  $\lambda^*$ , this confirms our findings.

There are a few differences to consider. We choose not to account for a possible redshift dependence. This is motivated by Bellagamba et al. (2019) finding only a shallow dependence, which they point out may be driven mainly by the highest redshift bin. Our lensing analysis employs a slightly different background selection for an increased source density, combined with a different derivation of the associated redshift distribution  $n(z)$ . Another difference is the inclusion of radial bins at  $0.1 \leq R < 0.2$  Mpc  $h^{-1}$ . This is expected to only have a minor effect, as the con-

tribution of the stellar mass is an order or magnitude lower than the halo term at these radii, while the contribution of miscentered halos only starts to become significant at larger radii (see also Rykoff et al. 2016; Oguri et al. 2018). In this sense, these findings are a confirmation of the robustness of the results across these papers.

### 5.2. Optimal estimators

Our results are in good agreement with paper I, with a relative bias between the two estimators that shows the recovered lensing signal is higher with LAD, suggestive of a lower absolute bias. At the same time, LAD regression gives a small (albeit significant) gain in efficiency, giving a reduction in error bars of a few percent, potentially up to 11% – 18% for shape measurements of a higher signal-to-noise ratio. LAD regression comes at the cost of a higher computation time, but at a step in the analysis process that does not dominate the total computational cost.

Both simulations (paper I) and analyses on real data (this article) cite quantitative results of significance, while at the same time showing similar trends between estimators on a qualitative level.

We have shown a cautious and thorough investigation, but can never exclude the unknown: biases arising due to assumptions in the simulations of Paper I or uncorrected systematic effects in this research, or, most likely, both. However, given the range and realism in simulated distributions and the similarities in findings among those simulations and this research and further literature, we are confident that the recovered differences in results between the two estimators are real.

We note some differences between the two analyses. In Paper I, we analyzed the regression of a sample of ellipticities with a single underlying value of the shear and, for each type of simulation, a single intrinsic ellipticity distribution. In this research, the situation is more complex. We studied the stacked signal around samples of lenses and of samples of background sources at a range of redshifts. This means also stacking noise that has been scaled by a range in lensing geometries, quantified by  $\Sigma_{\text{cr}}^{-2}$ . Furthermore, in each radial bin of each luminosity bin, we assume a constant lensing effect, which is in reality the stacked average of a range in  $L_{200}$ , and therefore a range in  $M_{200}$ , confounded by intrinsic scatter between these two quantities, and radial distance  $R$  from the lens, combined with miscentering of halos.

All these effects tend to convolve the intrinsic galaxy shape distribution, which makes the level of agreement and significance between the two papers in fact remarkably robust.

In conclusion:

- the combination of Paper I and this research show that LAD regression is more naturally suited to the cusped intrinsic ellipticity distribution of background galaxies;
- our simulations in Paper I showed a lower bias for LAD regression than for LSQ regression in the presence of noise in the background source shape measurements, whilst this research confirmed the same relative bias between the two estimators;
- constraints obtained via LAD regression are comparable or tighter than constraints obtained via LSQ regression.

An optimal estimator is, from a principled point of view, more objective and better suited than corrections to an approach, that is known to mismatch the sample distribution. More practically, LAD regression provides a robust consistency check for shear inference, which has been and still remains a major investment in the field of weak lensing. Keeping different perspectives, such

<sup>16</sup> e.g. Viola et al. (2015), where the group  $r$ -band luminosities are calculated by summing over spectroscopically confirmed group members.

as exploring these alternative statistical approaches, are fundamental in gauging the way forward.

**Acknowledgements.** MSm acknowledges support from the Netherlands Organization for Scientific Research (NWO). AD acknowledges ERC Consolidator Grant (No. 770935) LM acknowledges the grants ASI-INAF n. 2018-23-HH.0 and PRIN-MIUR 2017 WSCC32 “Zooming into dark matter and protogalaxies with massive lensing clusters”. MSe acknowledges financial contribution from contract ASI-INAF n.2017-14-H.0 and contract INAF mainstream project 1.05.01.86.10. Based on data products from observations made with ESO Telescopes at the La Silla Paranal Observatory under programme IDs 177.A-3016, 177.A-3017 and 177.A-3018, and on data products produced by Target/OmegaCEN, INAF-OACN, INAF-OAPD and the KiDS production team, on behalf of the KiDS consortium. OmegaCEN and the KiDS production team acknowledge support by NOVA and NWO-M grants. Members of INAF-OAPD and INAF-OACN also acknowledge the support from the Department of Physics & Astronomy of the University of Padova, and of the Department of Physics of Univ. Federico II (Naples).

## References

- Bacon, D. J., Refregier, A. R., & Ellis, R. S. 2000, *MNRAS*, 318, 625
- Barrodale, I. & Roberts, F. D. K. 1973, *SIAM Journal on Numerical Analysis*, 10, 839
- Bartelmann, M. & Maturi, M. 2017, *Scholarpedia*, 12, 32440
- Bartelmann, M. & Schneider, P. 2001, *Phys. Rep.*, 340, 291
- Begeman, K., Belikov, A. N., Boxhoorn, D. R., & Valentijn, E. A. 2013, *Experimental Astronomy*, 35, 1
- Bellagamba, F., Maturi, M., Hamana, T., et al. 2011, *MNRAS*, 413, 1145
- Bellagamba, F., Roncarelli, M., Maturi, M., & Moscardini, L. 2018, *MNRAS*, 473, 5221
- Bellagamba, F., Sereno, M., Roncarelli, M., et al. 2019, *MNRAS*, 484, 1598
- Benítez, N. 2000, *ApJ*, 536, 571
- Bernstein, G. M. 2010, *MNRAS*, 406, 2793
- Bernstein, G. M. & Armstrong, R. 2014, *MNRAS*, 438, 1880
- Bernstein, G. M. & Jarvis, M. 2002, *AJ*, 123, 583
- Bonnet, H. & Mellier, Y. 1995, *A&A*, 303, 331
- Brainerd, T. G., Blandford, R. D., & Smail, I. 1996, *ApJ*, 466, 623
- Bridle, S., Balan, S. T., Bethge, M., et al. 2010, *MNRAS*, 405, 2044
- Brouwer, M. M., Cacciato, M., Dvornik, A., et al. 2016, *MNRAS*, 462, 4451
- Cacciato, M., van den Bosch, F. C., More, S., Mo, H., & Yang, X. 2013, *MNRAS*, 430, 767
- Capaccioli, M. & Schipani, P. 2011, *The Messenger*, 146, 2
- Clampitt, J. & Jain, B. 2016, *MNRAS*, 457, 4135
- Coe, D., Benítez, N., Sánchez, S. F., et al. 2006, *AJ*, 132, 926
- Cooray, A. & Sheth, R. 2002, *Phys. Rep.*, 372, 1
- Cramer, H. 1946, *Mathematical Methods of Statistics* (Princeton mathematical series, Princeton University Press)
- Dark Energy Survey Collaboration, Abbott, T., Abdalla, F. B., et al. 2016, *MNRAS*, 460, 1270
- de Jong, J. T. A., Kleijn, G. A. V., Erben, T., et al. 2017, *A&A*, 604, A134
- de Jong, J. T. A., Verdoes Kleijn, G. A., Boxhoorn, D. R., et al. 2015, *A&A*, 582, A62
- de Jong, J. T. A., Verdoes Kleijn, G. A., Kuijken, K. H., & Valentijn, E. A. 2013, *Experimental Astronomy*, 35, 25
- Driver, S. P., Hill, D. T., Kelvin, L. S., et al. 2011, *MNRAS*, 413, 971
- Duffy, A. R., Schaye, J., Kay, S. T., & Dalla Vecchia, C. 2008, *MNRAS*, 390, L64
- Dvornik, A., Cacciato, M., Kuijken, K., et al. 2017, *MNRAS*, 468, 3251
- Erben, T., Hildebrandt, H., Lerchster, M., et al. 2009, *A&A*, 493, 1197
- Erben, T., Hildebrandt, H., Miller, L., et al. 2013, *MNRAS*, 433, 2545
- Erben, T., Schirmer, M., Dietrich, J. P., et al. 2005, *Astronomische Nachrichten*, 326, 432
- Evans, A. K. D. & Bridle, S. 2009, *ApJ*, 695, 1446
- Falk, M. 1997, *Annals of the Institute of Statistical Mathematics*, 49, 615
- Feigelson, E. D. 1988, *Bulletin d'Information du Centre de Données Stellaires*, 35, 197
- Feigelson, E. D. 2009, *arXiv e-prints*, arXiv:0903.0416
- Feigelson, E. D. & Babu, G. J. 2013, *Statistical Methods for Astronomy*, ed. T. D. Oswalt & H. E. Bond (Springer, Dordrecht), 445
- Fenech Conti, I., Herbonnet, R., Hoekstra, H., et al. 2017, *MNRAS*, 467, 1627
- Foreman-Mackey, D., Hogg, D. W., Lang, D., & Goodman, J. 2013, *PASP*, 125, 306
- George, M. R., Leauthaud, A., Bundy, K., et al. 2012, *ApJ*, 757, 2
- Giocoli, C., Marulli, F., Moscardini, L., et al. 2021, *A&A*, 653, A19
- Heck, A., Murtagh, F., & Ponz, D. 1985, *The Messenger*, 41, 22
- Herbonnet, R., Buddendiek, A., & Kuijken, K. 2017, *A&A*, 599, A73
- Heymans, C., Rowe, B., Hoekstra, H., et al. 2012, *MNRAS*, 421, 381
- Heymans, C., Van Waerbeke, L., Bacon, D., et al. 2006, *MNRAS*, 368, 1323
- Heymans, C., van Waerbeke, L., Miller, L., et al. 2012, *Monthly Notices of the Royal Astronomical Society*, 427, 146
- Hildebrandt, H., Choi, A., Heymans, C., et al. 2016, *MNRAS*, 463, 635
- Hildebrandt, H., Erben, T., Kuijken, K., et al. 2012, *MNRAS*, 421, 2355
- Hildebrandt, H., Viola, M., Heymans, C., et al. 2017, *MNRAS*, 465, 1454
- Hirata, C. & Seljak, U. 2003, *MNRAS*, 343, 459
- Hoekstra, H. & Jain, B. 2008, *Annual Review of Nuclear and Particle Science*, 58, 99
- Ivezić, Z., Kahn, S. M., Tyson, J. A., et al. 2019, *ApJ*, 873, 111
- Johnston, D. E., Sheldon, E. S., Wechsler, R. H., et al. 2007, *arXiv e-prints*, arXiv:0709.1159
- Kacprzak, T., Bridle, S., Rowe, B., et al. 2014, *MNRAS*, 441, 2528
- Kacprzak, T., Zuntz, J., Rowe, B., et al. 2012, *MNRAS*, 427, 2711
- Kaiser, N., Squires, G., & Broadhurst, T. 1995, *ApJ*, 449, 460
- Kaiser, N., Wilson, G., & Luppino, G. A. 2000, *arXiv e-prints*, astro
- Kautsch, S. J., Gonzalez, A. H., Soto, C. A., et al. 2008, *ApJ*, 688, L5
- Kitching, T. D., Balan, S. T., Bridle, S., et al. 2012, *MNRAS*, 423, 3163
- Kitching, T. D., Miller, L., Heymans, C. E., van Waerbeke, L., & Heavens, A. F. 2008, *MNRAS*, 390, 149
- Kuijken, K. 1999, *A&A*, 352, 355
- Kuijken, K. 2006, *A&A*, 456, 827
- Kuijken, K. 2011, *The Messenger*, 146, 8
- Kuijken, K., Heymans, C., Hildebrandt, H., et al. 2015, *MNRAS*, 454, 3500
- Lambas, D. G., Maddox, S. J., & Loveday, J. 1992, *MNRAS*, 258, 404
- Laureijs, R., Amiaux, J., Arduini, S., et al. 2011, *arXiv e-prints*, arXiv:1110.3193
- Leauthaud, A., Finoguenov, A., Kneib, J.-P., et al. 2010, *ApJ*, 709, 97
- Leauthaud, A., Massey, R., Kneib, J.-P., et al. 2007, *ApJ*, 172, 219
- Lesci, G., Marulli, F., Moscardini, L., et al. in prep., *A&A*
- Mandelbaum, R. 2018, *ARA&A*, 56, 393
- Mandelbaum, R., Rowe, B., Armstrong, R., et al. 2015, *MNRAS*, 450, 2963
- Massey, R., Heymans, C., Bergé, J., et al. 2007, *MNRAS*, 376, 13
- Maturi, M., Bellagamba, F., Radovich, M., et al. 2019, *MNRAS*, 485, 498
- McFarland, J. P., Verdoes-Kleijn, G., Sikkema, G., et al. 2013, *Experimental Astronomy*, 35, 45
- Mead, A. J., Peacock, J. A., Heymans, C., Joudaki, S., & Heavens, A. F. 2015, *MNRAS*, 454, 1958
- Melchior, P. & Viola, M. 2012, *MNRAS*, 424, 2757
- Miller, L., Heymans, C., Kitching, T. D., et al. 2013, *MNRAS*, 429, 2858
- Miller, L., Kitching, T. D., Heymans, C., Heavens, A. F., & van Waerbeke, L. 2007, *MNRAS*, 382, 315
- Miyatake, H., More, S., Mandelbaum, R., et al. 2015, *ApJ*, 806, 1
- Navarro, J. F., Frenk, C. S., & White, S. D. M. 1995, *MNRAS*, 275, 720
- Oguri, M., Bayliss, M. B., Dahle, H., et al. 2012, *MNRAS*, 420, 3213
- Oguri, M., Miyazaki, S., Hikage, C., et al. 2018, *PASJ*, 70, S26
- Oguri, M., Takada, M., Okabe, N., & Smith, G. P. 2010, *MNRAS*, 405, 2215
- Peacock, J. A. & Smith, R. E. 2000, *MNRAS*, 318, 1144
- Planck Collaboration, Ade, P. A. R., Aghanim, N., et al. 2014, *A&A*, 571, A16
- Radovich, M., Puddu, E., Bellagamba, F., et al. 2017, *A&A*, 598, A107
- Rao, C. R. 1945, *Bull. Calcutta Math. Soc.*, 37, 81
- Refregier, A. & Bacon, D. 2003, *MNRAS*, 338, 48
- Refregier, A., Kacprzak, T., Amara, A., Bridle, S., & Rowe, B. 2012, *MNRAS*, 425, 1951
- Rhodes, J., Refregier, A., & Groth, E. J. 2000, *ApJ*, 536, 79
- Robotham, A. S. G., Norberg, P., Driver, S. P., et al. 2011, *MNRAS*, 416, 2640
- Rodríguez, S. & Padilla, N. D. 2013, *MNRAS*, 434, 2153
- Rykoff, E. S., Rozo, E., Hollowood, D., et al. 2016, *ApJS*, 224, 1
- Schirmer, M. 2013, *ApJS*, 209, 21
- Schneider, M. D., Hogg, D. W., Marshall, P. J., et al. 2015, *ApJ*, 807, 87
- Schneider, P. 2003, *arXiv e-prints*, astro
- Schneider, P. 2006, in *Saas-Fee Advanced Course 33: Gravitational Lensing: Strong, Weak and Micro*, ed. G. Meylan, P. Jetzer, P. North, P. Schneider, C. S. Kochanek, & J. Wambsganss, 269–451
- Seitz, C. & Schneider, P. 1995, *A&A*, 297, 287
- Seitz, C. & Schneider, P. 1997, *A&A*, 318, 687
- Seljak, U. 2000, *MNRAS*, 318, 203
- Sellentin, E., Heymans, C., & Harnois-Déraps, J. 2018, *MNRAS*, 477, 4879
- Sifón, C., Cacciato, M., Hoekstra, H., et al. 2015, *MNRAS*, 454, 3938
- Smit, M. & Kuijken, K. 2018, *A&A*, 609, A103
- Tinker, J. L., Robertson, B. E., Kravtsov, A. V., et al. 2010, *ApJ*, 724, 878
- Tyson, J. A., Valdes, F., & Wenk, R. A. 1990, *ApJ*, 349, L1
- Valentijn, E. A., McFarland, J. P., Snigula, J., et al. 2007, in *Astronomical Society of the Pacific Conference Series*, Vol. 376, *Astronomical Data Analysis Software and Systems XVI*, ed. R. A. Shaw, F. Hill, & D. J. Bell, 491
- van den Bosch, F. C., More, S., Cacciato, M., Mo, H., & Yang, X. 2013, *MNRAS*, 430, 725
- van Uitert, E., Cacciato, M., Hoekstra, H., et al. 2016, *MNRAS*, 459, 3251
- van Uitert, E., Hoekstra, H., Joachimi, B., et al. 2017, *MNRAS*, 467, 4131
- Van Waerbeke, L., Mellier, Y., Erben, T., et al. 2000, *A&A*, 358, 30
- Verdoes Kleijn, G., de Jong, J. T. A., Valentijn, E., et al. 2012, in *Astronomical Society of the Pacific Conference Series*, Vol. 461, *Astronomical Data Analysis Software and Systems XXI*, ed. P. Ballester, D. Egret, & N. P. F. Lorente, 237
- Viola, M., Cacciato, M., Brouwer, M., et al. 2015, *MNRAS*, 452, 3529
- Viola, M., Kitching, T. D., & Joachimi, B. 2014, *MNRAS*, 439, 1909
- Voigt, L. M. & Bridle, S. L. 2010, *MNRAS*, 404, 458
- Wittman, D. M., Tyson, J. A., Kirkman, D., Dell’Antonio, I., & Bernstein, G. 2000, *Nature*, 405, 143



## Appendix A: Tests for systematics

For completeness, we reiterate some tests for systematics, that were already carried out in Dvornik et al. (2017); Bellagamba et al. (2019), because of our difference in sky coverage, background selection and estimated redshift distribution to either of these studies.

### Appendix A.1: Photometric redshift

We use the same method as Dvornik et al. (2017) to determine the comoving critical density. There are two important differences, that could affect the uncertainty in  $\Sigma_{\text{cr}}$ : we select lenses at a significantly higher redshift and we complement our background source selection with the color selection described in Section 3.2.

We assess the relative errors in  $\Sigma_{\text{cr}}$  by performing  $10^4$  bootstraps of the spectroscopic catalog of Hildebrandt et al. (2017). We find the median error on  $\Sigma_{\text{cr}}$  to be  $\sim 0.5\%$ , as shown in Fig. A.1.

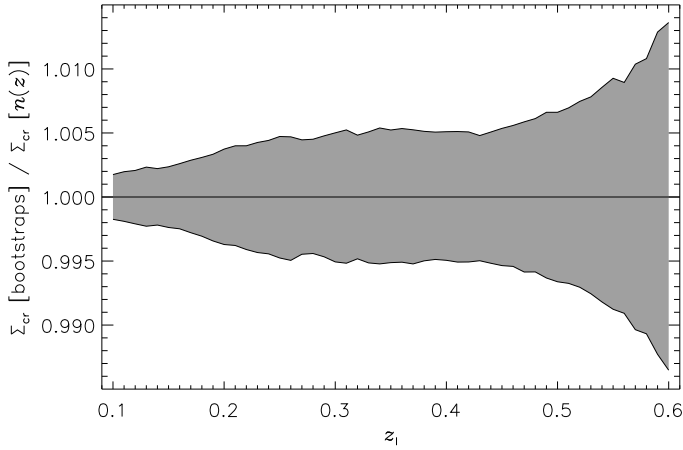


**Fig. A.1.** Relative errors in  $\Sigma_{\text{cr}}$ , estimated using  $10^4$  bootstraps of the spectroscopic catalog of Hildebrandt et al. (2017). The relative error on the ESD is negligible.

### Appendix A.2: Contamination of the background sample by cluster galaxies

Dvornik et al. (2017) showed that an offset of  $\Delta z = 0.2$  is enough to avoid a significant contamination of the background sources by unidentified GAMA group members. For lenses at a higher redshift, this contamination increases, while at the same time the density of available background sources decreases, due to the observed depth of KiDS-450.

We use the same test as Dvornik et al. (2017) to assess the source density around AMICO clusters, to determine the necessary  $\Delta z$  offset between lens and sources. We find that  $\Delta z = 0.2$  is appropriate for our cluster selection (Fig. A.2).

### Appendix A.3: Individual bin ESD profiles and cross signals

In Figure A.3, we show the ESD profiles for the 13 cluster bins, including the cross signal, which is consistent with zero. We also show the derived halo model fits and their confidence intervals, comparing the fits using the full AMICO cluster catalog from Fig. 7.

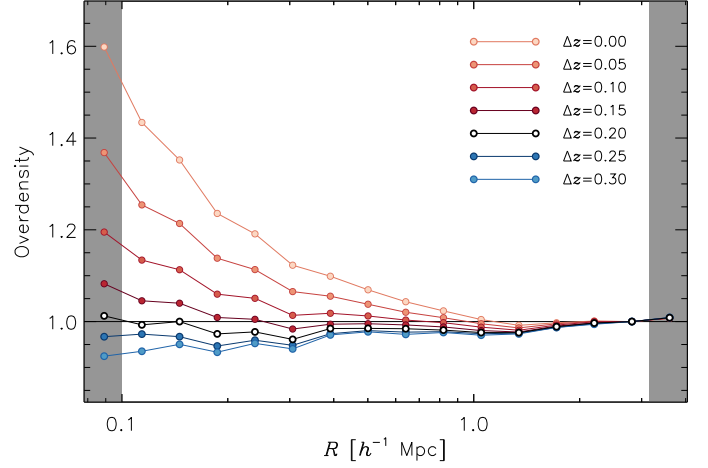


**Fig. A.2.** Relative source densities around AMICO clusters as function of radius  $R$  and photometric redshift offset  $z_B \geq z_l + \Delta z$  between lens and source. We note that some small underdensities around  $R = 0.2 h^{-1} \text{Mpc}$  may be due to the relative normalization.

### Appendix A.4: Tile bootstrap

As described in Section 3.3, we cannot use the same bootstrap approach as Dvornik et al. (2017), due to the sparsity of lenses in the highest lens luminosity bins. Since our bootstrap approach described in Section 3.3 does not account for cosmic variance and is not sensitive to the clustering effect of dark matter halos, we compare the covariances derived by the two bootstrap methods for the ESD of the whole lens selection in Fig. A.4, and find no significant differences or pattern, beyond what is expected from statistical noise. Since we expect the contribution from cosmic variance to be even lower for subsets of lenses, we conclude that our bootstrap approach yields a good estimate of the covariance.

## Appendix B: Analysis of dependency on outer data points

In Fig. 10, it can be seen that the distribution of clusters in two outermost luminosity bins is not symmetric. At the lower end, this is due to the selection criterion of  $\lambda^*$  in the AMICO catalog. At higher end, we have only few clusters.

We assess the effect these two points have on the  $L_{200} - M_{200}$  scaling relation, by repeating the fit without these bins. We find no difference within the statistical uncertainties, as given in Eq. B.1.

$$\text{Mean} \quad \frac{M_{200}}{10^{14.1} h^{-1} M_{\odot}} = (0.98 \pm 0.06) \left( \frac{L_{200}}{10^{11.8} h^{-2} L_{\odot}} \right)^{(1.25 \pm 0.10)}, \quad (\text{B.1a})$$

$$\text{LAD} \quad \frac{M_{200}}{10^{14.1} h^{-1} M_{\odot}} = (1.02 \pm 0.06) \left( \frac{L_{200}}{10^{11.8} h^{-2} L_{\odot}} \right)^{(1.23 \pm 0.09)}. \quad (\text{B.1b})$$



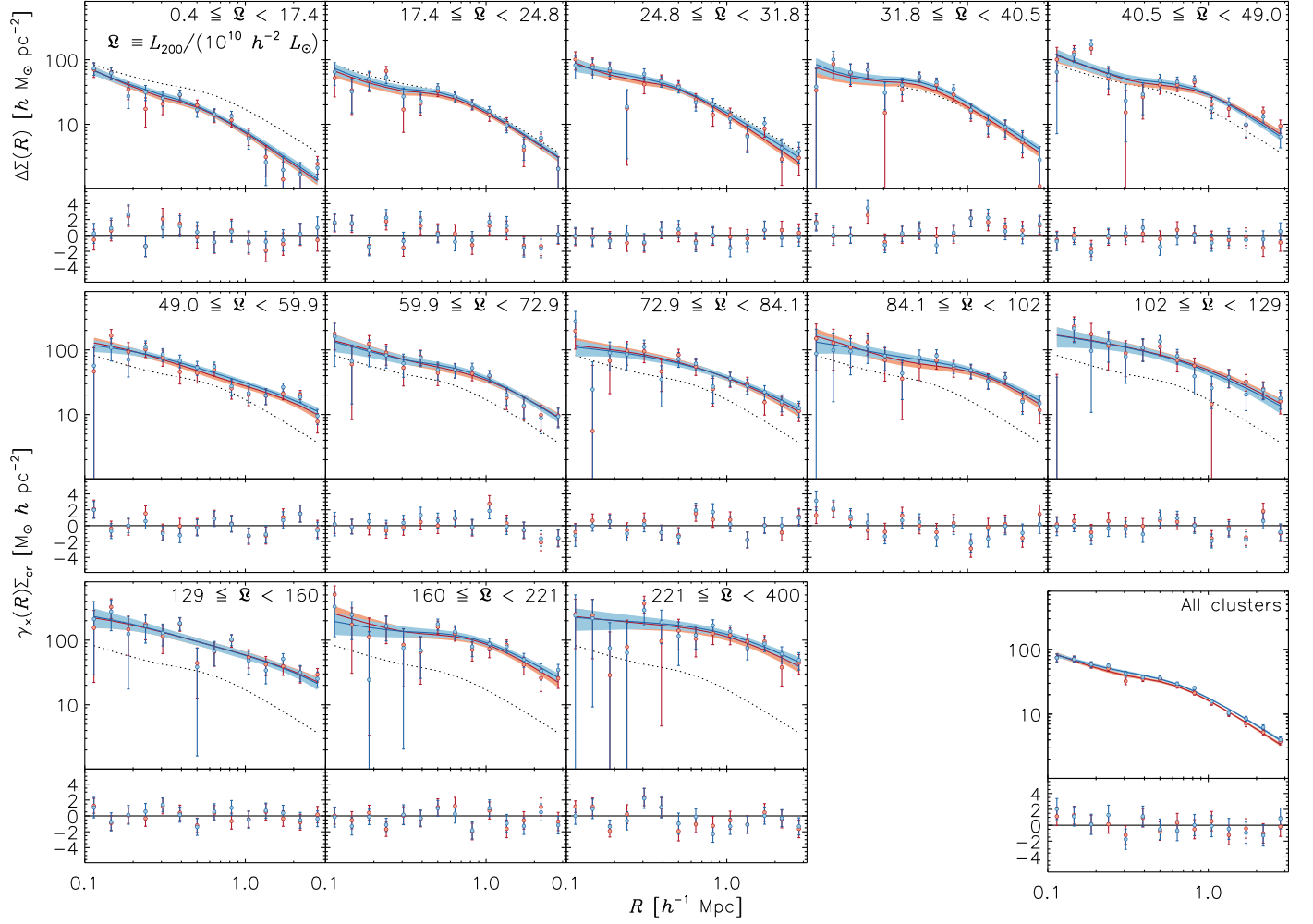


**Fig. A.3.** Estimated ESD profiles and cross signal of the 13 cluster bins, using the LAD estimator (blue) and a weighted mean (red). The error bars are the square roots of the diagonal values of the respective covariance matrices. The solid lines represent the best-fitting halo model obtained by the MCMC fit. The shaded regions show the 68.3% confidence bands, estimated using the 15.9th and 84.1th percentiles of the MCMC realizations. Individual bins are indicated by the range in normalized luminosity  $\Xi \equiv L_{200} / (10^{10} h^{-2} L_{\odot})$ . The lower right plot shows the ESD profile estimated from the full AMICO cluster catalog, also shown in Fig. 7. The average of the two best-fitting halo models from Fig. 7 are shown in each panel as a dotted line for easy comparison.

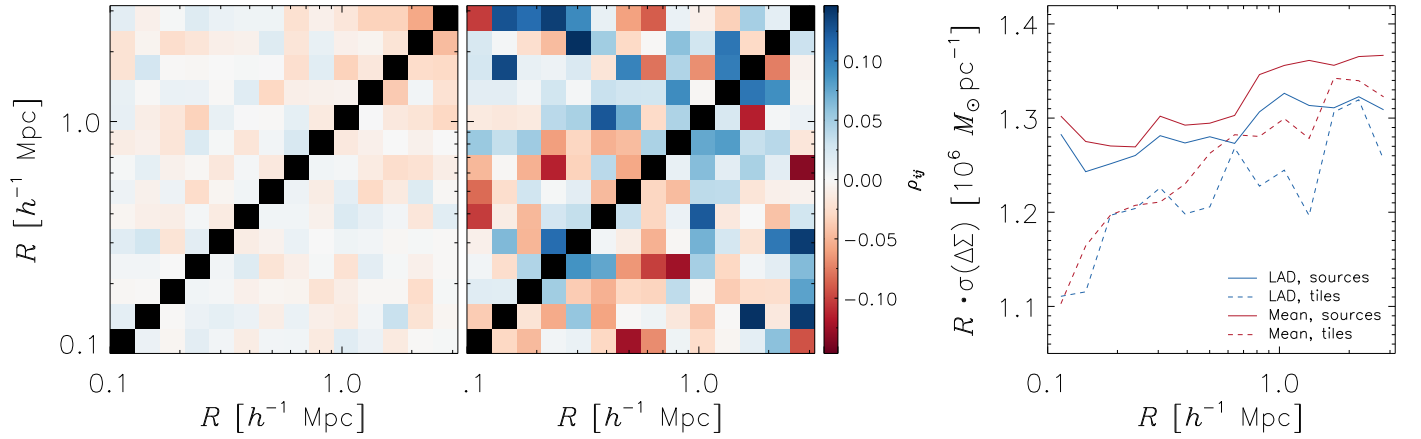


**Fig. A.4.** Left: Correlation derived from bootstrapping the signal by individual sources, same as Fig. 6, but with the color stretch adjusted to the middle plot. Middle: Correlation derived from bootstrapping the signal in  $1 \text{ deg}^2$  tiles. Upper left corners shows the correlations from LAD regression. Lower right corners show the correlations from using the weighted mean. Right: Comparison of the errors obtained from bootstrapping sources (LAD: solid blue, mean: solid red) and bootstrapping  $1 \text{ deg}^2$  tiles (LAD: dashed blue, mean: dashed red).